January 2018

Study Of Mri Signal In The Presence Of Discrete Spherical Magnetic Particles

Paul Kokeny
Wayne State University, eh5738@wayne.edu

STUDY OF MRI SIGNAL IN THE PRESENCE OF DISCRETE SPHERICAL MAGNETIC PARTICLES

by

PAUL KOKENY

DISSERTATION

Submitted to the Graduate School

of Wayne State University,

Detroit, Michigan

in partial fulfillment of the requirements

for the degree of

DOCTOR OF PHILOSOPHY

2018

MAJOR: BIOMEDICAL ENGINEERING

(imaging dual title)

Approved By:

_____

Co-Advisor Date

_____

Co-Advisor Date

_____

_____

_____

DEDICATION

I dedicate this dissertation to my advisors Dr. E Mark Haacke and Dr. Yu-Chung Norman Cheng. Without their guidance and support, I would have never been able to achieve what I have.

ACKNOWLEDGEMENTS

The majority of this work has been made possible through the financial support of the United States Department of Defense. I am also deeply thankful for my advisors Dr. Yu-Chung Norman Cheng and Dr. E Mark Haacke who made special considerations for me here based on some personal circumstances. I owe special gratitude to those who have helped me academically and intellectually throughout my time as a PhD student. Of course this starts with my advisors. Dr. Cheng and Dr. Haacke provided an excellent balance for me to learn to be careful and hard working, as well as creative and collaborative with my research. My other committee members have also helped me greatly to make it to this point. While it was easy for me to get lost in the technical and mathematical details of my research, Dr. Zhifeng Kou and Dr. Otto Muzik helped stress the importance of the big picture practical and clinical applications. I also owe a special thank you to Dr. Mehrmohammadi for his help when I had trouble with my committee.

Other faculty have also helped along the way. Mr. Yang Xuan and Mr. Zahid Latif assisted me greatly with phantom imaging and solving many of the technical problems that were encountered. Discussions with Dr. Matt Allen from the Chemistry Department at Wayne State University also helped solve some of the problems encountered during phantom development. His and Dr. Jena Bhanu's kindness in lending some materials from their labs was greatly appreciated. Dr. Quan Jiang from Henry Ford Hospital also helped by sharing animal data in a collaborative effort which led to my first paper.

I also must express a great deal of gratitude to other students and colleagues

whom I have spent time with during my PhD research. First, to Dr. He Xie and Dr. Ching-Yi Hsieh, who were also students of Dr. Cheng. Our weekly meetings were always helpful for solving problems, developing new ideas, and keeping a good pace of progress. Early on in my graduate schooling, Dr. Wei Feng and Dr. Jaladhar Neelavalli acted as mentors to me. Their technical knowledge in MRI set the benchmark for what I wanted to achieve. Last I would like to thank Mr. Ehsan Hamtaei, Dr. Saifeng Liu, Mr. David Utriainen, Mr. Sean Sethi, Dr. Uday Krishnamurthi, and Dr. Brijesh Yadav for helpful discussions about my research and MRI in general.

TABLE OF CONTENTS

LIST OF TABLES

LIST OF FIGURES

CHAPTER 1 MOTIVATION AND BASIC CONCEPTS

1.1 Motivation

Understanding and properly modeling magnetic resonance imaging (MRI) signal behavior under different conditions has led to some of the important advancements in the field. Modeling can be purely analytical or numerical in nature, allowing for the quantification and visualization of many different physiological factors; including blood flow, blood oxygenation, fat content, magnetic susceptibility, and diffusion. The better understanding and more accurate models we have, the more accurate such quantifications and visualizations can be, nonetheless limited by factors such as noise and partial volume.

Magnetic susceptibility is a material property that tells how magnetized an object becomes when placed in an external magnetic field. Given the high magnetic field strength of an MRI machine, even small susceptibility values can lead to appreciable field effects. Iron is ferromagnetic and carries a very high magnetization. Biological tissues can have varying magnetic susceptibility values based on their iron concentration. Such iron may be in the form of deoxyhemoglobin, ferritin, hemosiderin, or other molecules. Being able to accurately quantify susceptibility in the body allows for the quantification of iron concentration as they are linearly correlated. This is important for certain neurological diseases as they have been found to be associated with iron [1]. Magnetic susceptibility may be quantified using either magnitude or phase signal from MRI. Analytical models that depict a random distribution of paramagnetic spheres containing iron have been used to connect R_2^* and R_2 to susceptibility [2, 3]. On the other

hand, the Larmor equation states that phase information is proportional to the induced magnetic field. Since it is well understood how magnetized objects perturb the field around them, phase can be used to create entire susceptibility maps [4], or to perform quantifications on single objects with simple geometries as well [5, 6].

While it is well understood how a uniformly magnetized object creates magnetic field within and around it, most objects and tissues may not be uniformly magnetized. Rather, they contain many small discrete magnetic inclusions, with sizes usually on the order of molecules or cells. A vein, for example, consists of plasma mixed with discrete red blood cells which contain numerous hemoglobin molecules. Other tissues can have more complicated microsctructures. The white matter in the brain, for example, consists of microscopic cylindrical tracts called axons. Such a microsctructure leads to complicated macroscopic phase behavior and has been the focus of recent studies [7–10]. Even just spherical inclusions can lead to complex behavior when the potential for clustering is taken into account [11–13]. The necessity of proper modeling of microstructures, even for spherical inclusions, to explain the MRI signal behavior is the main focus of this dissertation.

This dissertation is organized into five major chapters. This chapter lays out the basic motivation and also goes into some more detailed technical background about MRI signal and its behavior in the presence of spherical magnetic inclusions. Chapters 2, 3, and 4 consist of original research projects. Chapter 2 focuses on developing a simulation based model of MRI signal in the presence

of spherical magnetic inclusions, with a focus on phase. Many simulation parameters were considered and some baseline criteria of parameters that lead to accurate simulations are presented. This chapter has already been published with myself as principal author [14]. Chapter 3 expands on the first work by performing simulations of long cylinders filled with spherical magnetic inclusions and comparing with experimental phantom data. It is shown that the resulting phase inside the cylinders can become non-linear, depending on particle arrangement, the number of particles per voxel, and Gibb's ringing, while the phase outside the cylinders has no such dependencies. At the time of submitting this dissertation, this chapter has been submitted for publication with myself as principal author. Chapter 4 provides an application of how the phase outside an object can be used to quantify iron tagged stem cells. This chapter has also been published with myself as principal author [15] Chapter 5 closes with some concluding remarks and potential future directions for the research.

1.2 Basic Concepts

The complex signal in MRI, in most cases, results from the transverse magnetization of hydrogen protons (or spins) from water molecules. Transverse refers to the plane perpendicular to the main MRI magnetic field. When hydrogen protons are exposed to an external magnetic field, their magnetization will align either parallel or anti-parallel to the external field and will also precess about the field at a frequency that is proportional to the external field strength. In fact, all nuclei and electrons will behave this way, yet hydrogen protons are the focus in MRI since their precession rate is in the radio frequency range that we can

safely interact with and the human body contains an ample amount in the form of water. Precession frequency is determined by the Larmor equation, given as $\vec{\omega} = \gamma\vec{B}$, where γ is the gyromagnetic ratio and $\vec{B}$ is the external field. For the hydrogen proton, γ is 2π42.58 MHz/Tesla. At room temperature, under exposure of typical strengths from the main magnetic field of an MRI machine, slightly more hydrogen protons will align parallel with the main field than anti-parallel, resulting in a net magnetization. In order to distinguish this net magnetization from the original much stronger external magnetic field, its direction must be changed. To accomplish this, a secondary magnetic field perpendicular to the main magnetic field, rotating at the same precession frequency as the hydrogen protons, is used to rotate the net magnetization toward the transverse plane.

Once tipped away from the main field, a transverse magnetization component is introduced. The secondary rotating field is then removed and a simple coil can be used to induce a measurable oscillating voltage from the transverse rotating magnetization. This magnetization is broken down into real and imaginary components by the process of demodulation. The rotating magnetization does not last forever, however. Due to interactions between spins, different spins will be subject to different magnetic field strengths, and according to the Larmor equation, will precess at different frequencies. The signal decay caused by this process is referred to as T_2 decay. On the other hand, inhomogeneities of the main external field and magnetic fields induced by any large magnetized inclusions will also influence the Larmor frequency over space. The signal decay due to these varying Larmor frequency is referred to as $T_2^{'}$ decay. These two different

signal decays together create what is referred to as T_2^* decay. Mathematically, the complex MRI signal, s, from the net transverse magnetization, neglecting coil sensitivity and some other factors, can be written proportionally as

$$s(t) \propto \int d^3r\, e^{-t/T_2} M_\perp(0) e^{i\gamma \Delta B_z(\vec{r})t} \tag{1.2.1}$$

where t is time, $M_\perp(0)$ is the initial transverse magnetization at $t = 0$, and the integration is performed over space. It is assumed that T_2 and initial transverse magnetization does not vary over space, and that the demodulated frequency is equal to the Larmor frequency of the hydrogen protons in the rotating frame, resulting in $\Delta B_z(\vec{r}) = B_z(\vec{r}) - B_0$ after demodulation. The integral of the entire $e^{i\gamma \Delta B_z(\vec{r})t}$ essentially leads to the $T_2^{'}$ decay caused by the varying $\Delta B_z(\vec{r})$ over space.

Let us now see what the T_2^* dephasing will be in the presence of a single magnetized spherical particle. From here out, the term "particle" will be used to represent a spherical magnetic inclusion. The component of the magnetic field along the external field direction induced by a single sphere with magnetic susceptibility χ, volume V_μ, radius R, subject to an external field strength B_0, is given by

$$\Delta B_{z,sphere}(\vec{r}) = \frac{\chi}{4\pi} V_\mu B_0 \frac{3\cos^2\theta - 1}{r^3} \quad \text{for}\, r > R \tag{1.2.2}$$

using spherical coordinates r and θ. Plugging this back into Eqn. 1.2.1 and ignoring the T_2 component gives

$$s(t) \propto 2\pi \int_0^{\pi} \int_R^{\infty} dr d\theta \, r^2 \sin\theta M_{\perp}(0) \exp\left(i\gamma \frac{\chi}{4\pi} V_{\mu} B_0 \frac{3\cos^2\theta - 1}{r^3} t\right) \quad (1.2.3)$$

While this equation neglects quite a few other factors on the signal, it demonstrates the point that $T_2^{'}$ can be tied to the magnetic susceptibility and the volume fraction of one or more particles.

Now imagine we have a single magnetized cylinder that has a uniform susceptibility χ and radius R, and is placed under an external field strength B_0, where the direction of the field and axis of the cylinder intersect at an angle θ. Assume this large cylinder occupies several voxels in an MRI image. The equation for the component of the induced magnetic field along the external field direction is given by magnetostatics, as

$$\Delta B_{z,out}(\vec{r}) = \frac{\chi}{2} B_0 \sin^2\theta \frac{R^2}{\rho^2} \cos 2\phi \quad \text{for } \rho > R \quad (1.2.4)$$

$$\Delta B_{z,in}(\vec{r}) = \frac{\chi}{2} B_0 (1 + \cos^2\theta) \quad \text{for } \rho < R \quad (1.2.5)$$

using cylindrical coordinates under the condition that χ is very small, which usually is the case in MRI applications (on the order of ppm). This is also under the assumption that the cylinder has a uniform and continuous susceptibility value. However, Equation 1.2.5 requires the Lorentz sphere correction, $-\frac{2}{3}\chi B_0$ (in SI units, which are used throughout this dissertation), in order to agree with experimental measurements. After the Lorentz sphere correction, the induced

field inside a cylinder is

$$\Delta B_{z,in}(\vec{r}) = \frac{\chi}{6} B_0(3\cos^2\theta - 1) \quad \text{for } \rho < R \tag{1.2.6}$$

On the other hand, if there are many additional magnetized spheres inside the cylinder, what would be the actual field, ΔB for the spin at position $\vec{r_0}$ inside the cylinder? One would have to take into account the fields from all particles, based on Eqn. 1.2.2. This would give

$$\Delta B_z(\vec{r_0}) = \sum_{i=1}^{N} \Delta B_{z,sphere}(\vec{r_0} - \vec{r_i}) \tag{1.2.7}$$

where $\vec{r_i}$ is the position of the i-th particle out of N total particles. If the number of particles is large, it is difficult and sometimes even impossible to model (although its necessity under certain conditions is the focus of this dissertation). Imagine instead that a pseudo spherical region with a radius on the order of several particles, centered at position $\vec{r_0}$, is selected. The field contributed from particles inside this spherical region is called the near field. The field contributed from particles outside this spherical region is called the far field. When there are sufficient number of particles outside this spherical region, the region can be treated as a continuous medium, and its contribution to the field at $\vec{r_0}$ can be determined from Eqn. 1.2.6.

If the field contribution from particles inside the spherical region leads to zero, then the overall field at position $\vec{r_0}$ is only the far field. In this case, the result is

Eqn. 1.2.6. The phase term of the MRI signal is

$$\phi(t) = \frac{\chi}{6}\gamma B_0(3cos^2\theta - 1)t \tag{1.2.8}$$

If there is enough spatial and temporal averaging of fields, the near-field contributions from particles will indeed cancel out. As a result, the phase value of the MRI signal due to many spherical particles inside a cylinder will agree with Eqn. 1.2.8. On the other hand, there are numerous scenarios where such cancellations will not occur. For example, if the atomic or molecular microstructures inside an object of interest has some complicated geometry, or if the temporal averaging of fields is not strong enough, these situations will not lead to cancellations of near-fields.

In MR applications, the sufficient averaging of fields will depend on the size, spacing, and magnetization of the inclusions that are mixed in with spins. In order for enough averaging to occur, the spin, on its path of diffusion, should be subject to a large variety of fields from inclusions. From this it is easily seen that smaller spacing, smaller size, and smaller magnetization will help this diffusion process. When the condition is met, this is referred to as the fast diffusion regime. On the other hand, when inclusions are large and further apart, diffusion will not lead to enough averaging and the fields induced by inclusions will dominate the signal behavior. This is referred to as the static dephasing regime.

In the static dephasing regime, with randomly distributed spherical particles, it has already been found from Eqn. 1.2.3 that an additional frequency shift

on top of Eqn. 1.2.6 will occur. But with different spatial arrangements of microstructures, the MRI signal will behave differently. The research in this dissertation focuses on spherical particle inclusions and how non-linear phase behavior, not able to be described by a single frequency shift, can arise. Phase outside the region of particles, however, will behave as if the object was a continuous medium, and Eqn. 1.2.4 will still be valid.

CHAPTER 2 A STUDY OF MRI GRADIENT ECHO SIGNALS FROM DISCRETE MAGNETIC PARTICLES WITH CONSIDERATIONS OF SEVERAL PARAMETERS IN SIMULATIONS

2.1 Introduction

Magnetic resonance imaging (MRI) signal behavior in the presence of magnetic particles has been of great interest. An understanding of this signal behavior from gradient echo images is important, as magnetic particles are related to nanoparticle labeled cells, contrast agents, and natural biological forms of iron such as ferritin and hemosiderin. Modeling the signals in the presence of such particles provides the first step of proper quantification of particle concentrations.

Quantification methods currently include R_2, R_2^*, or phase based methods such as quantitative susceptibility mapping (QSM). So far the models used to predict R_2 and R_2^* from magnitude signals are typically based on statistical methods that are evaluated either analytically [2], or numerically with Monte-Carlo simulations [16, 17]. While these models have considered the discrete particle nature of the system, modeling of phase values in QSM still assumes that a system with discrete particles behaves as a continuous medium [4, 18, 19]. Under the continuous medium assumption, phase should behave linearly over echo time. However, some recent work has shown that phase inside a system of particles can become non-linear from gradient echo images when all particles are included in the model [20]. This non-linearity deserves further studies. As we can imagine, if the concentration of particles is low in a system, it is understandable that modeling of the system to be a continuous medium is no longer

appropriate. An immediate question is how low the concentration is considered to be low. In addition, given the current computing capabilities, which are not sufficient to model trillions of particles in a simulation, it is also a question of at least how many particles should be included in a simulation.

In this work, simulation based models are used to investigate phase signals which depend on factors such as particle density, susceptibility, and particle distribution. In order to accurately represent actual systems of particles, careful considerations are made on the minimal size and the total number of particles in simulations. The $R_2^{'}$ relaxation rate will also be calculated and compared to theoretical estimates. In this first attempt to answer the questions that we want to investigate, only a small cubic field of view (FOV) will be utilized for simulations. Diffusion will not be considered in these simulations, as typically diffusion plays little role when nanoparticles are involved [21]. Thus our simulations will only be applicable to particle systems in the static dephasing regime [2]. Because of this, particle size in our simulations (given by the number of grid points it takes up in a 3D matrix) only reflects how well each particle will represent a perfect sphere. The bigger the particle is in our simulations, the more accurate the result. Our simulated results can represent MRI signals from magnetic particles in solutions or tissues that are actually in the static dephasing regime.

2.2 Theory

2.2.1 MRI Signal from a System of Particles

The induced magnetic field over space, $\vec{B}(\vec{r})$, due to a source of magnetization, $\vec{M}(\vec{r})$, can be written as

$$\vec{B}(\vec{r}) = \frac{\mu_0}{4\pi} \int_{V'} d^3r' \left\{ \frac{3\vec{M}(\vec{r'}) \cdot (\vec{r} - \vec{r'})}{|\vec{r} - \vec{r'}|^5} (\vec{r} - \vec{r'}) - \frac{\vec{M}(\vec{r'})}{|\vec{r} - \vec{r'}|^3} \right\} \tag{2.2.1}$$

where μ_0 is the permittivity of free space. If the magnetic susceptibility is a scalar, the induced field along the z-direction is

$$B_z(\vec{r}) = \frac{\mu_0}{4\pi} \int_{V'} d^3r' \left\{ \frac{3M_z(\vec{r'})(z - z')^2}{|\vec{r} - \vec{r'}|^5} - \frac{M_z(\vec{r'})}{|\vec{r} - \vec{r'}|^3} \right\} \tag{2.2.2}$$

This expression can be further rewritten as a convolution of the magnetization with a 3D Green's function G_{3D}

$$B_z(\vec{r}) = \mu_0 \int_{V'} d^3r' M_z(\vec{r'}) G_{3D}(\vec{r} - \vec{r'}) \tag{2.2.3}$$

where the Green's Function in spherical coordinates (r, θ, ψ) is

$$G_{3D}(\vec{r}) \equiv \frac{1}{4\pi} \cdot \frac{3\cos^2\theta - 1}{r^3} \tag{2.2.4}$$

For an object with a continuous magnetization, the above equation can be used to calculate the induced magnetic field inside and outside the object. However, in many practical situations, an object contains discrete ferromagnetic or superparamagnetic particles. Thus the integral in Equation 2.2.1 needs to be rewritten as a sum over particles, leading to

$$B_z(\vec{r}) = \mu_0 \sum_{i=1}^{N} \mu_i \cdot G_{3D}(\vec{r} - \vec{r_i}) \tag{2.2.5}$$

where μ_i is the relative magnetic moment of the i-th particle, defined as $\Delta\chi_i V_i B_0/\mu_0$, where $\Delta\chi_i$ is the susceptibility of the i-th particle relative to its surrounding, V_i is the volume of the particle, B_0 is the main field strength, and $\vec{r_i}$ is the position of the particle. Here It is important to note that, as the susceptibility $\Delta\chi_i$ is a relative term, so are the magnetization and magnetic moment used throughout the paper. The induced field in Equation 2.2.5 is the sum of fields from each individual particle, assuming that the total number of particles in this system is N. In addition, Equation 2.2.5 can be calculated through discrete Fourier transform, rather than directly adding Green's functions. Furthermore, if the object size is more than 50% of the FOV, and if discrete Fourier transform of the Green's function is not used, then Fourier transform can introduce sufficient errors in those calculations [5].

The complex MRI signal within a voxel obtained from a gradient echo sequence is found by convolving the true continuous signal with a sinc function. Each spin will precess at a frequency $\gamma B_z(\vec{r})$, where γ is the gyromagnetic ratio of the hydrogen proton, equal to $2\pi \cdot 42.58\,$MHz/T. The induced magnetic field $B_z(\vec{r})$ due to the susceptibility of the sample will vary over space according to Equation 2.2.5 and the reconstructed images in the Cartesian coordinates at a given echo time, TE, will be

$$\begin{aligned}&\hat{\rho}(x,y,z,TE)\\&\quad=\rho(x,y,z)\,e^{i\gamma B_z(x,y,z)TE}\\&\qquad*\left(\frac{1}{\Delta x\Delta y\Delta z}\frac{\operatorname{sinc}(\pi x/\Delta x)}{\operatorname{sinc}(\pi\Delta k_x x)}\frac{\operatorname{sinc}(\pi y/\Delta y)}{\operatorname{sinc}(\pi\Delta k_y y)}\frac{\operatorname{sinc}(\pi z/\Delta z)}{\operatorname{sinc}(\pi\Delta k_z z)}e^{-i\pi(\Delta k_x x+\Delta k_y y+\Delta k_z z)}\right)\end{aligned} \tag{2.2.6}$$

where ρ is the spin density, $*$ represents the convolution operation, Δx, Δy,

and Δz are image resolutions, and Δk_x, Δk_y, and Δk_z are the resolutions in k-space. The resolution in the image domain and k-space must satisfy the Nyquist criterion along each dimension. This reconstruction process is performed in our simulations following the diagram in Fig. 4.1.

2.3 Methods

Several factors need to be considered in our simulations. The general idea is to simulate sizable particles in a large matrix and to obtain images through reductions of the matrix size, according to the concept in MRI acquisition (Fig. 4.1). Each factor is discussed in each subsection below.

2.3.1 Simulation Procedures

Here we describe in detail of our simulation procedures, using Fig. 4.1 as a guide. We first set up magnetic field distributions from discrete particles. A large high-resolution 3D matrix is filled with particles, distributed and constrained within a given geometry of an object, which is further placed within a larger FOV. Magnetization of each particle is assigned to be $\Delta\chi B_0/\mu_0$. Magnetization is zero outside the particles. A discrete Green's function matrix of the same size is also needed to generate field values over the entire space. The center of the Green's function is assigned to be zero in order to include the Lorentz sphere correction [5]. The Fourier transform of both matrices is taken and then they are multiplied together in order to perform the convolution in Equation 2.2.3. The inverse Fourier Transform of this product provides a 3D matrix of magnetic field distributions. A slightly different but nearly equivalent way of generating fields from spherical particles is described in the Appendix. When the parti-

cle setup has even symmetry over each dimension (as we choose in the ground truth model described in Section 3.2), a discrete cosine transform rather than a fast Fourier transform can be used to generate field values. Compared to the usual fast Fourier transform, the cosine transform requires only 1/16 of the computer memory and number of computations for a 3D calculation. A phase matrix $\phi(\vec{r})$ is calculated from this field matrix by multiplying by γTE. To complete the complex signal calculation for the high resolution matrix, magnitude values have been assigned to unity both inside and outside the given geometry of the object, throughout the entire FOV. The magnitude and phase matrix together form one complex signal matrix $\rho(\vec{r})\, e^{i\phi(\vec{r})}$, where $\rho(\vec{r})$ and $\phi(\vec{r})$ are the magnitude and phase matrix, respectively. The Fourier transform of this high resolution complex matrix is then performed and only the central low frequency k-space portion, where its size matches the desired reconstructed MR image matrix size, is taken. The inverse Fourier transform is further performed on the central k-space portion, leading to a low resolution complex matrix which is our final image matrix. The ratio of initial to final matrix size is referred to as the "reduction ratio" here.

MATLAB and Fortran were used to perform all simulations in this work. For larger scale simulations that required over 16 GB of RAM, a Linux based computing system centralized in our university was used. This computing system contained 1.5 TB of RAM and utilized an Intel E5-2697v3 2.6 GHZ processor. For smaller scale simulations, a Windows based system was used with 16 GB of RAM and an AMD Phenom II X4 945 processor.

2.3.2 Particle Models

It is important to ensure that magnetic fields near every particle surface are set up accurately. While using a single point to represent each particle is desired so that computer memory may be conserved, a larger sphere to represent each particle may still be required for accuracy purposes. Here, one "point" simply refers to one element in a 3D matrix. In order to test the accuracy from different particle sizes, a "ground truth" model was developed for comparisons. In this model, spherical particles were simulated large enough so that they may represent perfect spheres. Our previous experience suggested that a radius of 32 points would be a suitable choice for each spherical particle [6]. A cubic 5120^3 FOV was set up with particles being contained in the central 3072^3 portion. A reduction ratio of 1024^3 was used resulting in a final matrix of 5^3 where the central 3^3 voxels contain all particles. The arrangement of 3^3 voxels was needed, as we had found out that particles in surrounding voxels will affect the MR signal in the voxel at the center, which is our voxel of interest. Empty voxels were added around the central 3^3 voxels, in order to avoid significant problems of aliasing from the Green's function [5]. This type of low resolution FOV was used for all simulations presented in this work, with only the reduction ratio changing when needed.

A total of 1728 large spherical particles were uniformly distributed within the central 3072^3 volume with a lattice arrangement, providing a volume fraction, λ, of 0.82%. The bulk susceptibility of the solution was defined as $\lambda\Delta\chi$ for all cases and was assigned to be 10/64 ppm. This led to a particle susceptibility

of roughly 19 ppm. The main magnetic field was assigned to be 3 T and was used for all simulations presented in this work. Echo times of 1 ms to 99 ms in increments of 2 ms were simulated using the procedures described above. These parameters, except for susceptibility values, were chosen to be similar to those in previous phantom experiments [22].

Several different particle sizes and shapes were compared to the ground truth model. These included using a single point, a 3^3 cube, and spheres of radii ranging from 2 to 5 and 16 points. In order to assign zero induced fields inside particles in some simulations, we chose an alternate method to generate fields (see 2.6). The matrix sizes of different models were reduced to the same desired matrix size by using different reduction ratios, in order to compare the ground truth to different particle models. Particle locations and distances were kept consistent for all models. For example, for the single point model which was 64 times smaller than the original ground truth size, all 1728 point particles were placed in the central 48^3 elements of a 80^3 high resolution matrix. The bulk susceptibility of the central 3^3 voxels was kept at 10/64 ppm. However, the volume fraction in this model was naturally increased to 1/64 due to the inherent volume differences between a cube and a sphere. A reduction ratio of 64^3 was used for this model. For the model with particle sizes of 3^3 cubes, we scaled up the single point model by a factor of 3 along each dimension, but kept all other parameters the same.

For other spherical particle models, the same lattice particle arrangement as in the ground truth was used, with every dimension scaled appropriately. The

bulk susceptibility was kept at 10/64 ppm in all cases and the volume fraction remained roughly the same as in the ground truth model, i.e., 0.82% (as we are using discrete points to create spherical particles, the volume fraction can change slightly for different particle sizes). The same echo times used in the ground truth model were simulated.

The phase values from the central voxel of each model and from all echo times were quantitatively compared to the phase values from the central voxel of the ground truth model, in order to determine which model is acceptable for further simulations.

2.3.3 Particle Susceptibility

Particle susceptibility in the ground truth simulation was varied from 1 ppm to 21 ppm in increments of 5 ppm, in order to determine the effect of particle susceptibility. As a result of the fixed volume fraction, the bulk susceptibility of the solution was no longer 10/64 ppm. All other parameters were kept the same. Since the phase value at any location in the matrix is proportional to the field and echo time, it is expected that varying particle susceptibility will have the same effect as scaling the echo time or field strength.

2.3.4 Particle Density and Distribution

Lattice and quasi-random arrangements were used to determine the effect of particle distributions. Quasi-random arrangements of particles would provide a uniform distribution and avoid problems such as pockets of increased and decreased particle densities [23]. Particles were modeled as spheres with a radius of 4 points based on results from above simulations. Quasi-random

arrangements were created by allowing each particle to be randomly placed within a cubic sub-volume. The center of each cubic sub-volume followed a lattice arrangement within an object described below. This concept is illustrated in Fig. 2.2. Sub-volumes with sizes of 8^3, 16^3, 24^3, and 32^3 points were used. In addition, in order to simulate 27, 216, and 1728 particles per voxel within the central 3^3 voxels in low resolution images, the particles were first generated within the respective central 288^3, 576^3, and 1152^3 points (i.e., the object) in high resolution matrices, and the entire FOV of each setup was downsized with reduction ratios of 96, 192, and 384, respectively. These setups led to the same volume fraction of roughly 0.82%. In addition, particles with lattice arrangements were also generated within the central 3^3 voxels of low resolution images. In each "sub-volume type" of the particle distribution with three different particle densities (i.e., number of particles per voxel), except for the lattice arrangement of particles, 30 different particle arrangements were simulated. A bulk susceptibility of 10/64 ppm was again used. Here only echo times from 1 ms to 49 ms in increments of 2 ms were used in order to reduce the computational time. The resulting magnitude and phase value from the central voxel in each arrangement were analyzed.

2.3.5 Volume Fraction

Only a quasi-random arrangement of particles with a sub-volume type of 24^3 points was used to test the effect of volume fractions. The bulk susceptibility was kept constant at 10/64ppm, while the number of particles was changed to 172 and 344 per voxel such that the volume fraction of particles was either 5%

or 10%. A reduction ratio of 96^3 and particles with a radius of 4 points were used.

2.3.6 Continuous Medium

A simulation of a continuous medium (rather than discrete particles) was performed, with the central 1536^3 points of a 2560^3 FOV having a bulk susceptibility of 10/64 ppm. A reduction ratio of 512^3 was used. As a result, the central 3^3 voxels out of the 5^3 FOV in low resolution images were filled by the continuous medium. The purpose of this simulation is to show the differences between discrete particle models and a continuous medium model.

2.3.7 Field of View

As mentioned above, when the ratio of the region containing particles to FOV is large, some errors can be introduced into results [5]. Thus it is important to make sure that the size of the FOV is large enough, in order to avoid significant errors. To test the effect of FOV on our simulations, we repeat the simulations with a quasi-random arrangement with a sub-volume type of 24^3 points and extend the FOV from 5^3 to 7^3 voxels in low resolution images, for particle densities of 27 and 216 particles per voxel in the central 3^3 voxels.

2.4 Results

Results from the ground truth model demonstrate that phase behavior deviates from the results of a continuous medium. Phase values from the ground truth model are nonzero at most echo times (Fig. 4.2), while the phase value from the center of a continuous cubic medium should be zero. The $R_2^{'}$ value of 86.8 Hz calculated from the ground truth model is also higher than 50.5 Hz

predicted from the static dephasing regime by Yablonskiy and Haacke [2]. This is likely due to the lattice arrangement of particles which breaks the assumption of randomness.

The phase as a function of echo time from other particle models, along with the ground truth are shown in Fig. 4.3. It is seen that a particle radius of at least 4 points leads to results comparable to the ground truth, up until an echo time of roughly 70 ms. The percentage errors between the two models are mostly within 10%. The single point particle and cubic model do not lead to good results and they are not shown in Fig. 4.3. Beyond the echo time of 70 ms, the inaccuracy of the induced fields near the surface of each particle becomes noticeable in our simulations. In fact, when the echo time is very long and/or the particle susceptibility is very high, such that phase values around each particle are too large, it is a question whether the particle radius is large enough to properly model the phase outside. This question arises when we observe erratic phase curves at long echo times. However, as the dephasing effect around a particle becomes strong in these conditions, a small particle size with large phase values around the particle is equivalent to a large particle with small phase values around the particle. Even with this interpretation, when the phase value outside a particle becomes large, say, 10π, a 10% error can significantly change the phase signal. With the proper size of particles used in simulations, the bulk phase values averaged from 30 different particle arrangements for each sub-volume type seem to be non-linearly proportional to the echo time (Fig. 4.4), yet different than the nonlinear behaviors shown by [20].

Even with the MR signal given by Equation 2.2.6, varying particle susceptibility seems to only scale the phase plot in the time dimension. This indicates that particles of different susceptibilities may be simulated by adjusting the echo times of any other susceptibility appropriately. However, it is important to note that, when the induced phase outside each particle is too small, the accuracy of the phase value at each point again becomes more important. As a result, particles must be modeled much larger, in order to achieve accuracy.

The effect of particle density and distribution on phase behavior from the central voxel as a function of echo time is shown in Fig. 4.4. The averaged phase values from 30 quasi-randomly arranged particle distributions for each sub-volume type and particle density are shown. Error bars at each echo time represent one standard deviation. Two general trends can be seen. First, as the particle density in each sub-volume type with a fixed volume fraction increases, the variance in the resulting phase behavior decreases. The average over 30 arrangements for each particle density shows a strong agreement when the number of particles per voxel is at least 216, suggesting that the average from these simulations can be used to predict results from even more particles per voxel with a fixed volume fraction. Second, phase behavior seems to depend on the sub-volume type of the particle distribution. As locations of particles become more and more restricted, in the case of quasi-random arrangements, the phase behavior first shows more biased toward negative values and then eventually begins to resemble the results from the lattice arrangement. When using a lattice arrangement, the final signal behavior does not show any dependence on the number of particles present

within a voxel.

This same trend is observed from increasing the volume fraction of particles, as long as the bulk susceptibility is kept the same. Including more particles in the system within the same FOV simply reduces the variance in the phase. For the simulated volume fractions of 5% and 10%, the averaged phase values remain in very good agreements. However, keeping the same particle susceptibility while increasing the volume fraction will increase the bulk susceptibility and thus different phase values.

It was found that $R_2^{'}$ is much more sensitive to the sub-volume type of the particle distribution than particle density. As particle distributions become less random, $R_2^{'}$ begins to increase and deviate away from the theoretical prediction of 50.5 Hz. Within the same sub-volume type of the particle distribution, the variance of R2' is much lower than the variance of its corresponding phase pattern. The distributions of $R_2^{'}$ values for each sub-volume type are shown in Fig. 2.6a. The signal decay of a quasi-random distribution with a sub-volume type of 24^3 points shows a contradiction to the results from [21]. The natural log of the magnitude signal decay becomes less linear, indicating bi-exponential decays, as the particle density increases. This can be seen in Fig. 2.6b.

In the case of a continuous medium, the resulting phase from the center of the FOV is nearly zero over all echo times, which is different from results of discrete particles. Thus a continuous medium cannot be substituted by discrete particles in the same system.

The FOV size has a much larger effect on phase from the 27 particles per voxel

simulation than the 216 particles per voxel simulation, as shown in Figs. 2.7a and 2.7b. While the shapes of averaged phase curves as a function of echo time seem to be different slightly between the two FOVs, the differences are within the one standard deviation. However, such high variances suggest that we should use high particle densities in future simulations. The effect of FOV on $R_2^{'}$ was much less. Using 27 particles per voxel, the 5^3 and 7^3 FOV resulted in $R_2^{'}$ values of 57.3 Hz and 56.8 Hz, respectively. Using 216 particles, the 5^3 and 7^3 FOV resulted in R2' values of 56.6 Hz and 54.4 Hz, respectively.

We have also compared the density of states between different particle arrangements and densities. Density of states is calculated in each case by taking the one dimensional Fourier transform of the complex signal over echo time from the central voxel of the cubic FOV. For each type of arrangements, the averaged density of states and the standard deviation at each point is plotted in Fig. 2.8. For a highly random particle arrangement, the density of states becomes symmetric and appears to resemble a Lorentzian distribution. However, as the particles become more restricted, the density of states starts to lose its symmetry and leads to a bi-exponential decay of the MR magnitude signal.

If an MR magnitude signal shows a mono-exponential decay over time, its density of states should follow a Lorentzian distribution in the frequency domain. Simulations of random particle arrangements in [21] with high particle densities have shown a Lorentzian distribution. However, our simulations using their particle densities indicate that this should not be the case (see the bi-exponential decay in Fig. 2.6b). This discrepancy is possibly due to the use of very small

particle sizes in [21]. As we have shown in Fig. 4.3, the particle radius needs to be simulated at a minimal size. Otherwise the phase outside each particle will not be accurate enough to give correct MR signals.

2.5 Discussion

The above results suggest that, even when a high particle density is randomly distributed, there may be an underlying bias in the resulting bulk phase behavior in the static dephasing regime. This indicates that the near field around each particle must be properly calculated. The fields at these locations will be dominated by near-by particles. Such a bias in the phase behavior could possibly pose a problem for applications of phase based quantification methods such as QSM, which assumes a continuous medium and thus no such biases.

Our results also suggest that lower particle densities introduce nonzero phase values with high variances in the central voxel of cubic systems over echo time. This observed variance is caused by the unique arrangement of individual particles in voxels and the lack of spatial averaging of fields. As more particles are added into the system, there is more spatial averaging occurring and the variance is reduced. Thus this variance will likely only be a problem when the entire system has low numbers of particles. On the other hand, our results indicate that it is suitable to use only 1728 particles per voxel to represent even more particles with the same volume fraction in simulations.

If only a single voxel with particles was used in simulations, phase and R2' values were significantly different than those shown in Figs. 4.4 and 2.6a. Extending the 3^3 voxels to larger cubic volumes did not make a significant difference,

indicating that an additional single layer of voxels around the central voxel is sufficient to demonstrate our results.

As our simulations do not include diffusion, they are only applicable to systems of particles in the static dephasing regime. The condition for this regime is given by Yablonskiy and Haacke [2] as

$$\delta\omega\frac{R^2}{6D} \gg \lambda^{-\frac{1}{3}} \tag{2.5.1}$$

where $\delta\omega$ is the equatorial frequency deviation at the surface of a particle, R is the radius of the particle, D is the coefficient of diffusion for spins, and λ is the volume fraction of the particles in the system. It was noted in [21] that cells labeled by SPIO (superparamagnetic iron oxide) may satisfy the criteria required for the static dephasing, as long as they are large enough or have high enough magnetizations. This has been shown to be the case with most iron-oxide loaded cells [24].

The phenomenon of non-cancelling near fields around each particle will only affect the phase values inside the region where particles occupy. The fields outside the particle region will still be induced from the combined far-fields of all particles. This outside field may also be used to quantify the magnetic moment of the object and it may be a more robust method since any near-field effects will not exist.

The R_2' value is less susceptible to variations in particle arrangements within the same sub-volume type, as long as the distribution is quasi random and the

particle density is high enough. This is somewhat expected since a fundamental assumption in the analytical treatment from Yablonskiy and Haacke [2] is a random arrangement with a uniform distribution. As more restriction of particle arrangements is introduced into a system, the R2' value increases. As a result, a lattice arrangement of particles has the highest R2' value. This concept is likely the cause of the extremely large R2* values observed from frozen tissues, on the order of 1000 Hz [25], where the increased spatial order in the system is more directly from water molecules than from particles in water.

Another aspect of this work is to show the importance of choices of simulation parameters. It is found that a particle radius of at least 4 points should be used, with the field strength, susceptibility values, and echo times chosen in our simulations. The FOV should be large enough compared to the object of interest, in order to avoid aliasing of the phase due to Fourier transforms used in simulations. It is also important that a sufficient particle density such as 1728 particles per voxel is better to be used. If the susceptibility value of each particle or echo time is more than an order of magnitude different than that used in our above simulations, then the ground truth model should be re-simulated for comparisons, in order to ensure the correctness of the model with smaller particle sizes.

2.6 Conclusion

When predicting phase behavior from a system of particles, the assumption of a continuous medium may be invalid in the static dephasing regime. When a large number of particles are present in the system, as would be more likely in

a practical application, our results suggest that there will be a phase bias inside the system over echo time. This bias may affect quantitative methods that are based on phase information estimated from the continuous medium model. We find that this bias arises from fields around particles. If the particles in a system are more randomly distributed, R_2' will decrease and approach to the predicted value from the static dephasing theory. However, phase values as a function of echo time are not predicted by the same theory.

Appendix: Generating Fields with Modeling Particles in the Magnetization Matrix versus in the Green's Function Matrix

The typical method of generating magnetic fields or phase from Equation 2.2.3 is to set up the geometry of objects and convolve the geometry with the Green's function, as described under Section 2.3.1. This method defines the object geometry in the magnetization matrix. However, if objects are a group of identical spheres, the described method of generating fields would be equivalent to the following procedure: the geometry of spherical objects can be replaced by their centers (i.e., single points), and the size of the sphere is defined in the Green's function, with nonzero Green's function values outside the sphere but with zeros inside the sphere in the Green's function. The convolution between the geometry and the Green's function will still lead to the correct field maps.

This alternate method of simulation was first tested in the ground truth, with spherical particles of a radius of 32 points. The results from these two different procedures are shown in Fig. 2.9. The differences between two results for echo times less than 70 ms are less than 2.5%.

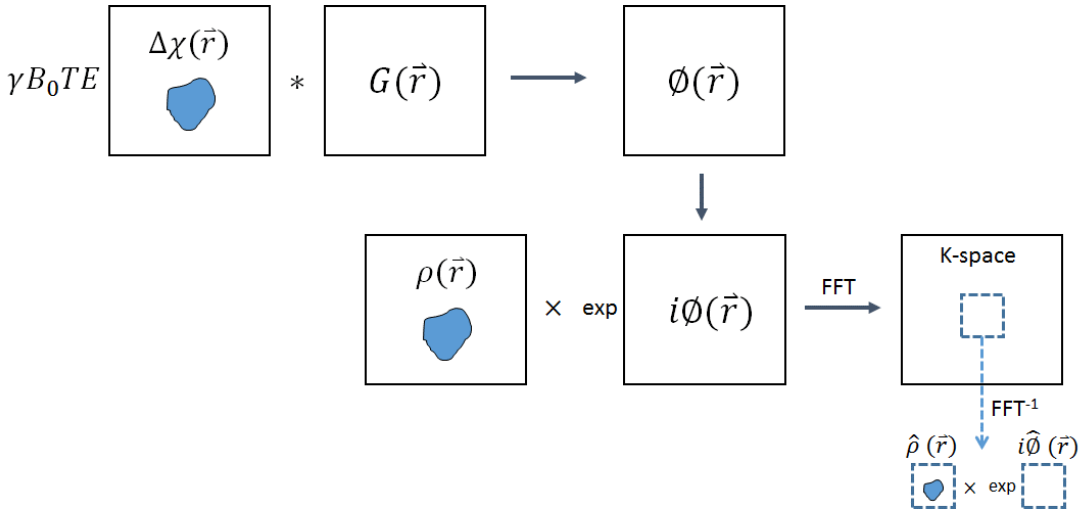

Figure 2.1: A schematic representation of the procedure used for simulating MRI complex signals. Convolution of a large 3D magnetization matrix and the Green's Function is used to create a high resolution phase matrix. Combining the phase matrix and a spin density matrix creates a high resolution complex signal matrix. This matrix is cropped in k-space to reach a final desired image resolution.

Using this alternate method allows us to simulate fields from a group of random spherical particles faster. In addition, if simulated particles are not perfect spheres, this alternate method ensures the induced field is zero inside particles, but the induced field inside non-spherical particles will not be zero in the method using the magnetization matrix.

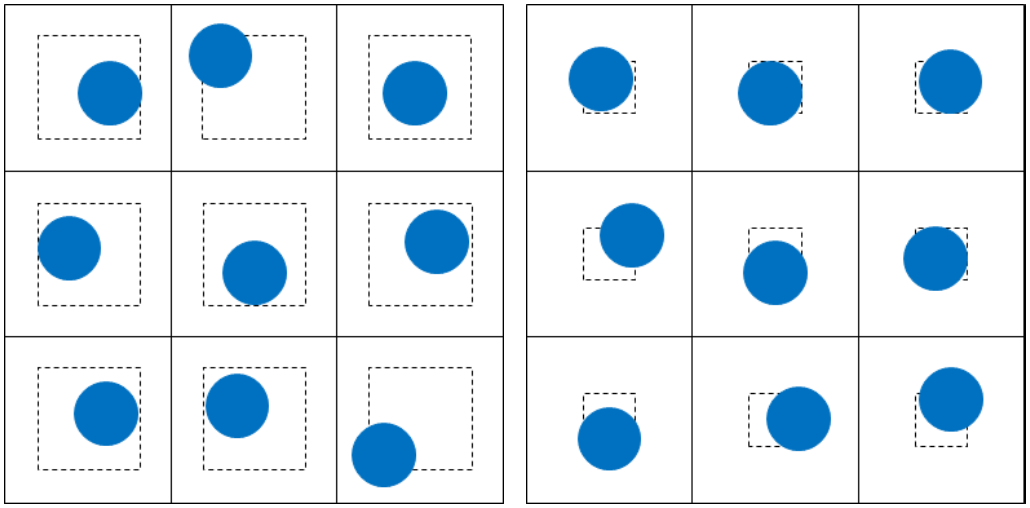

Figure 2.2: Two different sub-volume types of particle arrangements. Each sub-volume type is defined by the size of the dashed box within each cell. The center of each particle is randomly placed inside each dashed box. The center of each dashed box follows the lattice arrangement inside the 3^3 voxels (i.e., the object).

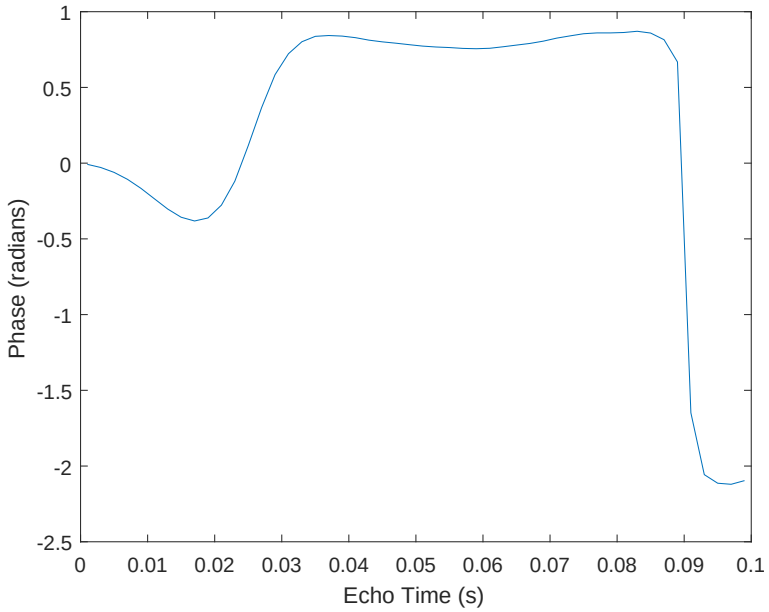

Figure 2.3: Phase at the central voxel of the ground truth model plotted as a function of echo time.

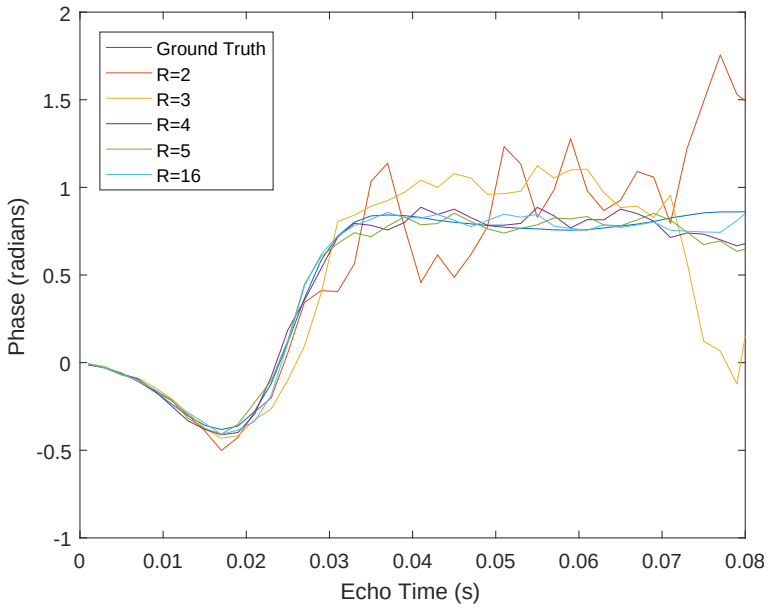

Figure 2.4: Phase from using a lattice arrangement of spherical particles with radii of 2, 3, 4, 5, and 16 points, compared to the ground truth which uses a radius of 32 points for each particle.

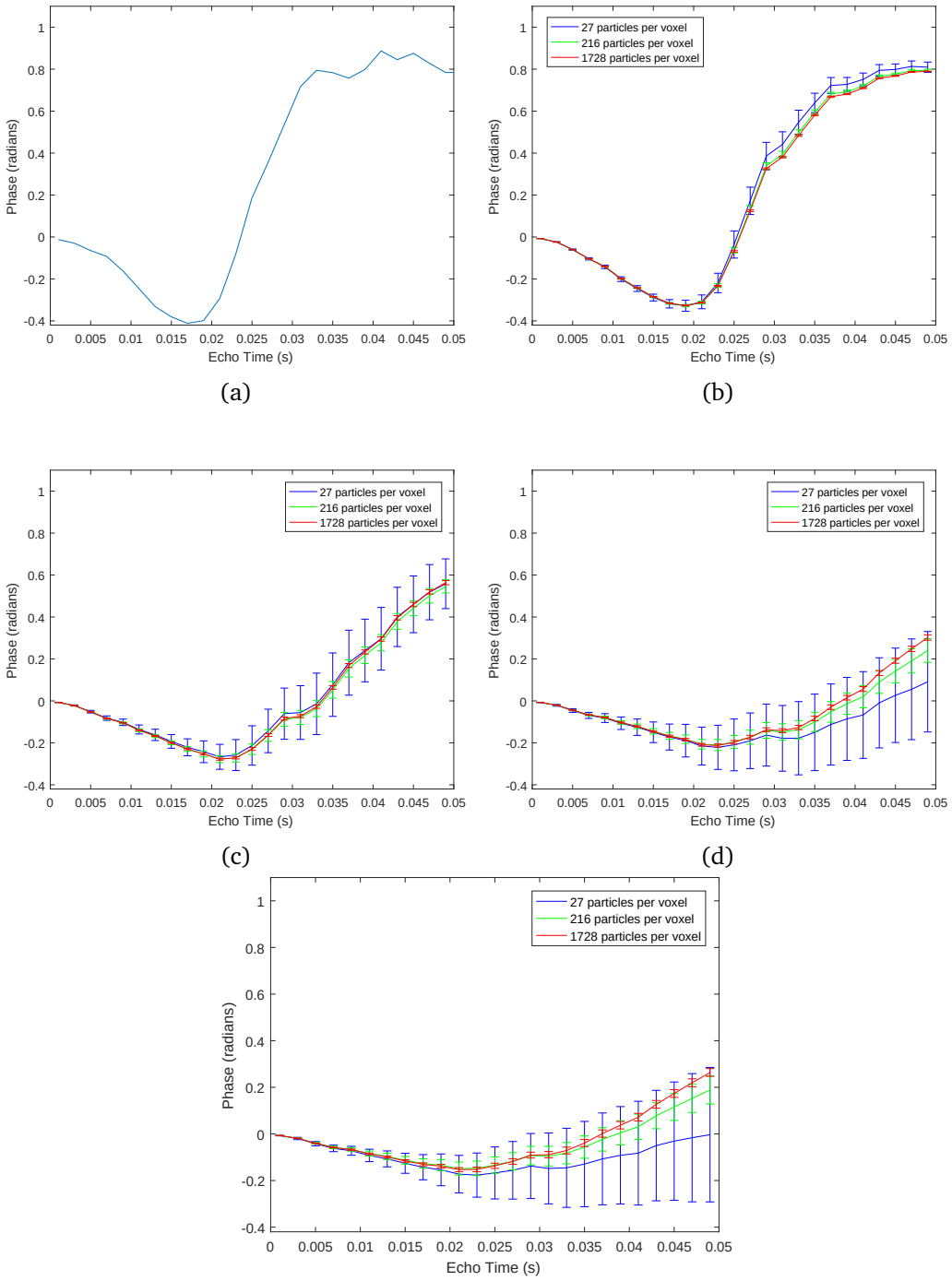

Figure 2.5: Phase values at the central voxel of the cubic FOV averaged from (a) lattice arrangement, (b) 30 different quasi-random arrangements with a sub-volume of 8^3 points, (c) 30 different quasi-random arrangements with a sub-volume of 16^3 points, (d) 30 different quasi-random arrangements with a sub-volume of 24^3 points, and (e) 30 different quasi-random arrangements with a sub-volume of 32^3 points. Each type of arrangement has 3 different particle densities; 27, 216, and 1728 particles per voxel. Error bars represent one standard deviation from the 30 arrangements. A particle radius of 4 points has been used in these simulations.

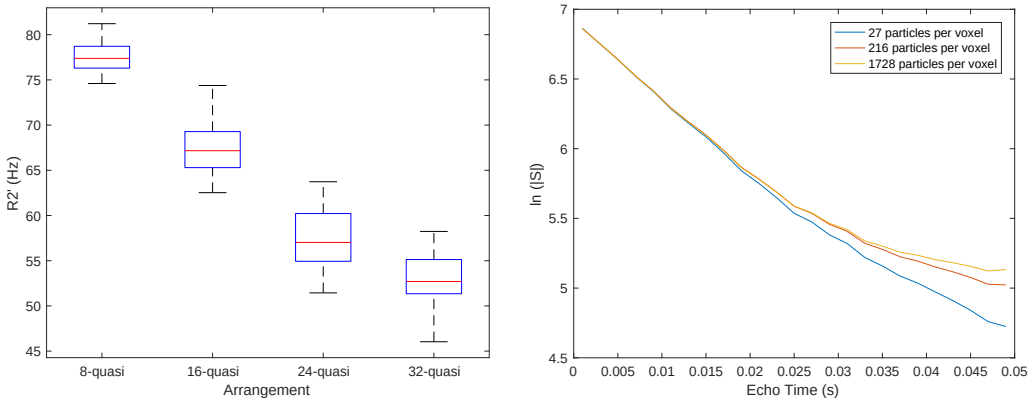

(a) (b)

Figure 2.6: (a) The distributions of $R_2^{'}$ values for all different sub-volume types of quasi-random arrangements. A particle density of 27 particles per voxel is used here. Increasing the particle density will reduce the variance of each measured $R_2^{'}$ value. When the order of the arrangement increases, so does the $R_2^{'}$ value. (b) The natural log of the averaged signal decay is shown for three particle densities from a quasi-random distribution. As the particle density increases (but with a fixed volume fraction), the curve becomes less linear.

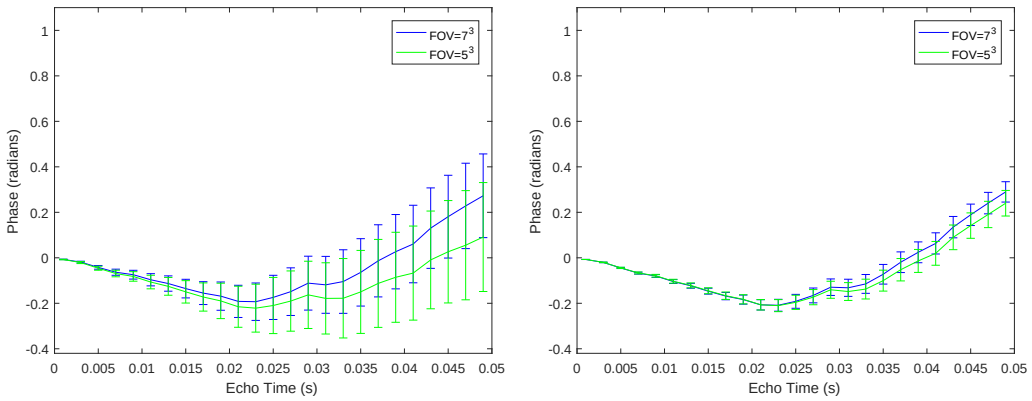

(a) (b)

Figure 2.7: A comparison of the averaged phase from the central voxel between two different FOVs: 5^3 and 7^3 voxels. Thirty quasi-random arrangements of particle locations were simulated for each FOV and for a particle density of (a) 27 particles per voxel and (b) 216 particles per voxel.

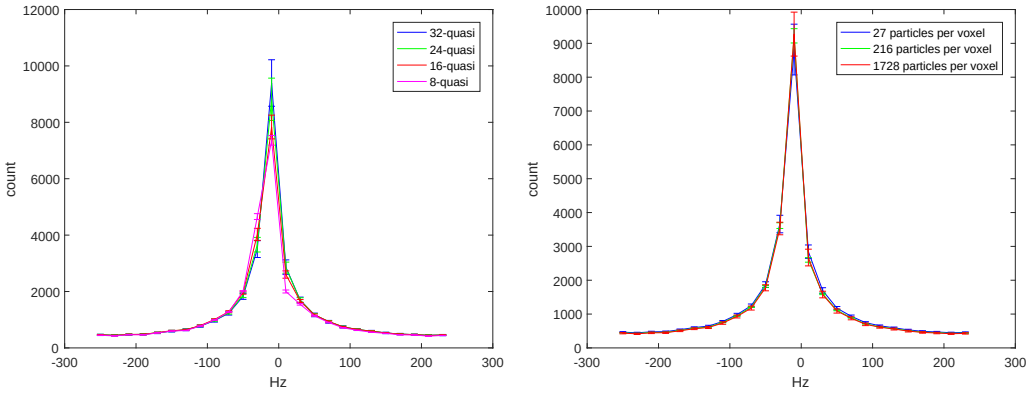

(a) (b)

Figure 2.8: (a) The averaged density of states for all different sub-volume types of quasi-random particle arrangements. As the order of the arrangement increases, the density of states starts to deviate away from a Lorentzian shape. (b) The density of states for three different particle densities with a sub-volume type of 24^3 points for the particle arrangement. As the particle density increases, the variance of the density of states decreases.

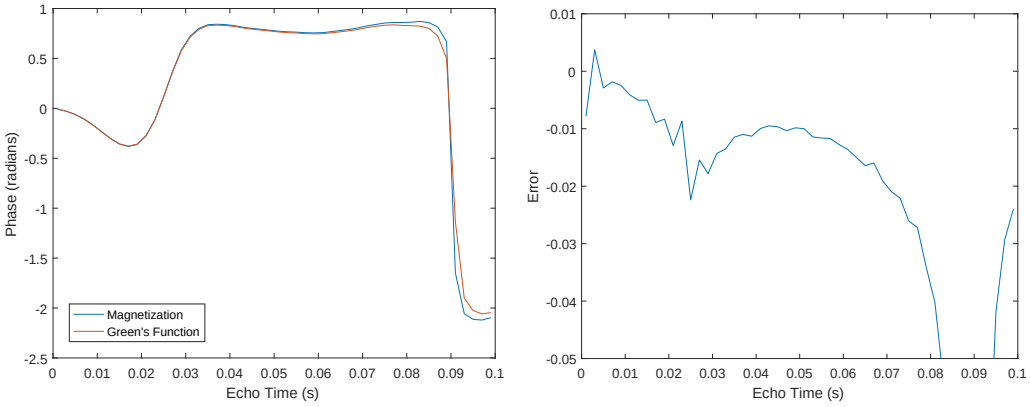

(a) (b)

Figure 2.9: Two methods of generating data from the ground truth model, described in the Appendix are shown in (a). For the conventional method, the entire spherical particle is defined in the magnetization matrix. For the alternate method, the particle size is defined in the Green's function matrix. The errors between the two curves are shown in (b).

CHAPTER 3 MIXTURES OF DISCRETE SPHERICAL PARTICLES WITH A CONSTANT SUSCEPTIBILITY CAN LEAD TO ECHO TIME DEPENDENT PHASE SHIFTS

3.1 Introduction

Phase and magnitude information from magnetic resonance imaging (MRI) can be used for both the visualization and quantification of magnetic susceptibility. This is important clinically as the susceptibility of biological tissue is directly related to iron content or other sources such as calcium. Iron content in the brain is of interest as it has been associated with several diseases [1]. Quantitative susceptibility mapping (QSM) has also been an active research topic [26, 27].

In most applications, an object or a tissue consists of numerous discrete magnetic inclusions rather than a purely uniform continuous medium. While induced magnetic fields from all these inclusions should be used to calculate the complex MRI signal behavior of the object, due to the current computational limitations, it has been convenient to treat the object as a continuous medium, especially for calculations of MRI phase values. However, it has been shown that the phase signal from the white matter does not agree with the model from a uniform medium, due to the microstructure such as axons in the white matter [9, 28, 29].

From a different consideration in physics, magnetic field calculations from a macroscopic object containing numerous discrete magnetic inclusions should include a far-field and a near-field contribution, in addition to the Lorentz sphere correction. The far-field contribution can always be considered from an equivalent bulk susceptibility of the macroscopic object containing inclusions [30].

The near-field contribution is zero, for a continuous medium with an isotropic susceptibility. For discrete spherical inclusions, the near-field is also zero if the fast diffusion condition is met [13, 19]. However, in the static dephasing regime where diffusion is neglected, the near-field contribution is not zero, as shown from nuclei magnetic resonance (NMR) frequency shifts in [13] with a theoretical background described in [2].

As the frequency shift in NMR determined from [13] would imply echo-time independent results, while our previous simulations of particles in cubes [14] have shown echo-time dependent phase values from MRI, this major discrepancy requires further investigations. In this work, the main goals are to (1) simulate gradient echo MR images from Fe_3O_4 nanoparticle solutions and from mixtures of polystyrene beads in gel, (2) analyze how several factors (the number of particles per voxel, the arrangement of particles, Gibb's ringing, etc.) from simulations can affect phase values, and (3) compare results to experimental data (nanoparticles and beads) and current theories (Eqn. 3.2.2 and Eqn. 3.2.3 below).

3.2 Methods

3.2.1 Background

The analytical work done by [2] on randomly distributed spherical particles within a large sphere has predicted a first-order frequency shift $\Delta\omega$ in the static dephasing regime.

$$\Delta\omega = -0.053\gamma B_0 \lambda \Delta\chi \tag{3.2.1}$$

where B_0 is the main field strength, λ is the volume fraction of particles, $\Delta\chi$ is the magnetic susceptibility of the particles relative to their surrounding, and γ is the gyromagnetic ratio of the hydrogen proton with a value of $2\pi \cdot 42.58$ rad/s/T. In NMR where cylindrical test tubes are used for containing discrete magnetic inclusions, Ruh et al. [13] had expected such a frequency shift in addition to the original NMR frequency shift. On the other hand, an infinitely long cylinder with a uniform magnetic susceptibility $\Delta\chi'$ has the following phase inside the cylinder.

$$\phi_{in} = \gamma B_0 T_E \Delta\chi' \left[\frac{3\cos^2\theta - 1}{6}\right] \tag{3.2.2}$$

where $\Delta\chi' = \lambda\Delta\chi$ is the bulk susceptibility of the cylinder, T_E is the echo time and θ is the angle between the axis of the cylinder and the main field. The left-handed system is adopted for the sign convention used in Eqn. 3.2.2.

In either phantom or in vivo studies, which involve numerous magnetic inclusions inside long cylinders, most work so far has modeled those long cylinders with uniform susceptibility values and used Eqn. 3.2.2. That is appropriate for the fast diffusion regime [13]. However, for the static dephasing regime where diffusion is neglected, results from [13] have suggested the following phase value inside a cylinder consisting of numerous discrete spherical particles when $\lambda < 0.2$.

$$\phi_{in} = \gamma B_0 T_E \lambda\Delta\chi \left[\frac{3\cos^2\theta - 1}{6} - 0.053\right] \tag{3.2.3}$$

The second term in Eqn. 3.2.3 may act as a near-field contribution to the original phase term (i.e., the far-field contribution). One of our goals here is to examine the validity of Eqn. 3.2.3.

3.2.2 Experiments

3.2.2.1 Fe_3O_4 Nanoparticles

In our previous work [22], we have prepared and imaged a phantom containing four different susceptibility values of nanoparticle solutions in plastic straws (0.29, 0.56, 1.11, and 2.20 ppm). Each straw had an inner radius of 2.98 ± 0.03 mm and an outer radius of 3.20 ± 0.03 mm. Images were acquired from an 11-echo susceptibility weighted imaging (SWI) sequence on a 3 T Siemens Verio machine with the straws perpendicular and parallel to the main field. The imaging parameters relevant to our simulation parameters provided later were: 1 mm isotropic resolution, 2.89 T actual main field, and T_E ranging from 5.68 ms to 29.58 ms in increments of 2.39 ms. The image matrix size was 256×256 with 64 slices. Data from the first echo time of 5.68 ms or the highest susceptibility were not used, as either the phase effect was too small to measure or the dephasing effect was too heavy to maintain the signal-to-noise ratios (SNR). All other data were re-used in this work.

3.2.2.2 Polystyrene Beads

In addition to the existing nanoparticle data, we conducted an experiment using large 90 μm diameter polystyrene spherical beads (Polysciences, Inc.) and gel doped with Gd-DTPA (0.5 M Magnevist). This doped gel acted as a reference in terms of susceptibility, and was used to mix with beads inside a plastic straw

and to surround the straw as well. In this experiment, three identical 7-oz plastic cups were used in order to remove background phase and the susceptibility effect from the straw itself. Cup 1 consisted of a straw filled with polystyrene beads and doped gel, surrounded by doped gel. Cup 2 consisted of a straw filled with and surrounded by doped gel. Cup 3 only had doped gel. The phantom construction procedure is as follows.

A single straw with the same dimensions used in the nanoparticle experiment was cut in half and glued to the bottoms of Cups 1 and 2. Distilled water of 600 ml and Magnevist of 36 ml were mixed together and heated to roughly 40° C using a hot plate. At this point, 15 g of gelatin powder was added and the whole solution was mixed uniformly. This concentration should lead to a susceptibility relative to water of about 9.4 ppm according to the molar susceptibility of Gd-DTPA [31]. With a reported magnetic susceptibility for polystyrene relative to water of -0.26 ppm [32], this would lead to a susceptibility difference of about -9.66 ppm between polystyrene and the doped gel (However, later our results show this was not the case). Roughly 312,000 polystyrene beads (about 0.12 ml in total volume) was added to 3 ml of doped gel, resulting in a volume fraction of about 3.8%, and transferred to the straw in Cup 1. This led to roughly 100 beads per mm^3. Another 3 ml of gel with no beads was transferred to the straw in Cup 2. The remaining doped gel solution was then poured into all three cups outside the straws, all to the same height. All three phantoms were then covered and placed in a refrigerator to solidify.

MRI imaging was performed on a Siemens 3T Verio system with a single loop

6 cm diameter eye coil. In order to properly remove the background phase, it was important that all 3 cups were imaged in the exact location relative to both the main magnet and eye coil. To achieve this, we secured the eye coil to a fixed position relative to the patient table. This allowed for each cup to be placed directly into the eye coil where the increasing diameter of the cup allowed it to sit firmly with the coil half way up the cup. For the parallel orientation, only the reference cup (Cup 3) and Cup 1 were needed to be imaged. In this orientation, each cup was secured on its side and the eye coil was laid flat onto the cup's side.

The SWI sequence was used for imaging, with a TR of 37 ms and 6 echo times from 8.19 ms to 31.79 ms in increments of 4.72 ms. The read bandwidth per pixel was 219 Hz. A 1 mm isotropic resolution was used and the total matrix size was $128 \times 128 \times 64$. When the straw was perpendicular or parallel to the field, the imaging orientation was coronal or transverse, respectively. As T_1 of the high concentration Gd-DTPA was significantly shortened, a flip angle of 80° and 6 averages of images were used to help increase the SNR.

3.2.3 Simulation Procedures

In each simulation, we calculate magnetic fields and MRI signals from a distribution of spherical particles inside a finite cylinder (which is shown in Fig. 3.1), centered within a 3D rectangular field of view (FOV). Each simulated case corresponds to beads or nanoparticles inside a straw used in experiments. We try to match as many simulation parameters to experimental values as possible. These include echo times, cylinder diameter, center of the cylinder at the sub-voxel

location, magnitude signal ratio between inside and outside the cylinder (in order to match the Gibb's ringing), bulk susceptibility, and number of particles per voxel for polystyrene beads. However, as the volume fractions of nanoparticle solutions are very low, which leads to very large grid sizes that cannot be handled with current computer memory, higher volume fractions are used in our nanoparticle simulations. As we have found out from our previous work [14], as long as the bulk susceptibility and particle arrangement are the same, varying the volume fraction and particle susceptibility (in the range of 1 to 20 ppm) leads to the same phase shifts as a function of echo time. In the end, 4 different bulk susceptibilities (1 for polystyrene beads and 3 for nanoparticles) have been simulated at orientations both perpendicular and parallel to the main field. Each simulated case has been re-generated multiple times using different seed values for the random number generator to produce different particle arrangements.

The basis of our simulation procedures have been described in [14]. Briefly, the magnetic field distributions will be added from contributions of each individual spherical particle on a 3D high-resolution matrix. This process of addition is circumvented by the convolution of the 3D Green's function and the geometry of all particles. The high-resolution field data are then converted to phase values. A separate high-resolution spin density grid, in which the values inside particles are set to zero but set to unity outside them, is combined with phase values to form a high-resolution complex grid. The low-resolution magnitude and phase images are created through a Fourier transform of the high-resolution complex grid, a cropping in k-space (with its size described below), and an inverse Fourier

transform of the cropped grid. Due to the large scales of these simulations, several modifications have to be made in order to conserve computer memory and computation time.

The first modification utilizes the far-field and near-field concept. Regions of particles far from a region of interest can be treated as a continuous medium. Based on this concept and the linear summation of magnetic fields, an infinitely long cylinder containing discrete particles can be decomposed to a combination of a short cylindrical section containing particles and an infinitely long cylinder filled by a continuous medium, with a subtraction of the same short section from the continuous medium. This is illustrated in Fig. 3.1. The field distributions calculated in the middle cross sectional plane of the cylinder will be analyzed.

The second modification takes advantage of the 3D even symmetry of the Green's function and of the finite cylinder in the rectangular FOV. As a cosine Fourier transform performed on one half of a function with even symmetry is equivalent to performing a fast Fourier transform on the entire function, the use of a cosine Fourier transform on one half of the FOV in all three dimensions saves a factor of 16 in computation time and memory. However, as a result, the particles will only be randomly placed within one octant of the cylinder, and then reflected over other octants. This is shown in Fig. 3.2. Included in the saved computation time, the actual reflection process only needs to be performed after the high-resolution complex grid is cropped in k-space. A fast inverse Fourier transform is then applied to the reflected k-space data and the final low resolution images of the entire FOV including the cylinder are reconstructed.

Third, we tried to mimic the Gibb's ringing from experiments by measuring magnitude signals inside and outside each straw at every echo time, and then matching these values in simulations. The center of each straw in the experiment was obtained from the Complex Image Summation around a Spherical or a Cylindrical Object (CISSCO) method [5] with sub-voxel accuracy, which was also matched in simulations of cylinders by adding the appropriate linear phase in k-space, in order to create a sub-voxel shift in the spatial domain.

Three different particle placement methods were used: one for purely random particle arrangements, one for quasi-random particle arrangements, and a lattice arrangement. For the purely random arrangements, particles were first randomly placed throughout the entire high resolution grid, ensuring that no overlap of particles would occur. For the quasi-random arrangements, each particle was constrained to a volume of 34^3 grid points and allowed a random placement within a smaller cubic sub-volume. This idea was described in more detail in [14]. Cubic sub-volume sizes of 8^3, 14^3, and 26^3 were used. After all particles were placed, one octant of a cylinder was defined at the corner of the high resolution matrix and all particles outside this cylinder were removed. In a separate simulation, the exact same octant of the cylinder filled by a continuous medium was defined and was used to generate field distributions as described above in the first modification.

In all simulations, the radius of each spherical particle was chosen to be 4 grid points in the high-resolution matrix [14] and this choice led to a volume of 257 grid points. The susceptibility value of each particle was set to be the desired

bulk susceptibility of the cylinder (quantified from experimental data) divided by the volume fraction of the particles. The final low-resolution matrix size of the entire FOV was $16 \times 16 \times 40$ and the final short cylinder had a radius of 3 pixels and a length of 20 slices. The size of the high-resolution matrix depended on the desired number of particles per voxel and their volume fraction, whose information are provided below. A main magnetic field of 2.89 T was used for all simulations, as this was the actual field strength of our Siemens 3 T Verio system. Echo times used in simulations were matched with their corresponding values in experiments.

Fortran was used to perform all simulations. A Linux based computing system centralized in our university was used. This computing system allowed for the use of up to 1.5 TB of RAM and utilized an Intel E5-2697v3 2.6 GHZ processor.

3.2.3.1 Other Simulation Details for Fe_3O_4 Nanoparticles

The volume fractions were chosen somewhat arbitrarily; lower than 20% so Eqn. 3.2.3 might be valid [13]. All simulations for nanoparticle concentrations used 1728 particles per voxel. For particles randomly distributed inside cylinders, volume fractions of roughly 2.8%, 5.2%, and 11.8% were chosen for the bulk susceptibilities of 0.29, 0.56, and 1.11 ppm [22], respectively. These values led to relatively consistent particle susceptibilities of roughly 10.4 ppm, 10.8 ppm, and 9.4 ppm, respectively, which also fell within the range of susceptibility values tested in [14]. The corresponding high-resolution grid sizes were $2016 \times 2016 \times 5040$, $1632 \times 1632 \times 4080$, and $1248 \times 1248 \times 3120$. With the respective crop factors of 252^3, 204^3, and 156^3 applied to the central por-

tion of k-space, these high-resolution matrices were reduced to achieve the final $8 \times 8 \times 20$ low-resolution matrices ($16 \times 16 \times 40$ after reflecting over each axis). Two different random particle arrangements were simulated and averaged for each bulk susceptibility and cylinder orientation, in order to improve the accuracy of the results. For the largest grid size, each arrangement took about 48 hours to simulate results from all 10 echo times. A set of simulated images are shown in Fig. 3.3.

Only one quasi-random particle arrangement for the bulk susceptibility of 0.29 ppm with the cylinder perpendicular to the main field was simulated, as it was found to agree better with the experimental results than the purely random arrangement. This simulation used a high resolution grid size of $1904 \times 1904 \times 4760$ and a crop factor of 238^3, in order to satisfy a multiple of the 34^3 unit volume used in our quasi-random arrangements. The cubic sub-volume was 26^3 grid points. In this case, the resulting volume fraction was 3.3% and the particle susceptibility was about 8.8 ppm.

3.2.3.2 Other Simulation Details for Polystyrene Beads

All simulations for polystyrene beads used 125 particles per voxel. For particles randomly distributed inside cylinders, a volume fraction of roughly 3.7% and a particle susceptibility of roughly -6.5 ppm were used. These values led to a bulk susceptibility of roughly -0.24 ppm, measured from experiments using procedures described below. The high-resolution grid size was $760 \times 760 \times 1900$ and the crop factor was 95^3. For quasi-random arrangements, as each particle was allowed to move within a unit volume of 34^3 grid points, this led to a crop

factor of 170^3, a volume fraction of roughly 0.65%, and a high-resolution grid size of $1360 \times 1360 \times 3400$. As a result, the particle susceptibility was roughly 37 ppm, which fell outside the range tested in [14]. All 3 cubic sub-volumes sizes of quasi-random arrangements and an additional randomly distributed arrangement with the 0.65% volume fraction were used for simulating polystyrene beads. In all these simulations, 16 arrangements were simulated and averaged for each cylinder orientation, in order to effectively get closer to the desired 1728 particles per voxel and improve the accuracy of our results.

3.2.4 Data Analysis

For all experimental and simulated results, we would like to quantify the bulk susceptibility of each cylinder using only the phase outside, containing only far-fields from particles, to determine the SNR and phase values inside the cylinder at each echo time, and to calculate R_2^*. Uncertainties were estimated using the error propagation method. Procedures of these tasks are described below.

3.2.4.1 Experimental Data from Fe_3O_4 Nanoparticles

Archived and processed complex images of nanoparticles in water from [22] were re-analyzed. Sixteen pixels of each slice over the 9 central slices inside the straw were averaged at each echo time for perpendicular and parallel orientations. The means and standard deviations (i.e., image noise) of both magnitude intensities and phase values were calculated from those 144 voxels, which also included Gibb's ringing effects. Thus, SNRs were estimated from magnitude images and each R_2^* was determined by performing linear regression on the natural log of magnitude intensities over three echo times from 8.07 ms to 12.85 ms.

Phase data from any echo time with an SNR less than 3:1 were omitted from the results. With the known diameter of the straw, the CISSCO method was applied to processed phase images in order to determine the bulk susceptibility and sub-voxel center of each straw from the perpendicular orientation.

3.2.4.2 Experimental Data from Polystyrene Beads

The phase distributions inside each cup but outside each straw were measured and symbolically expressed by:

$$\begin{aligned} \phi_{cup1} &= \phi_{bkg} + \phi_{straw} + \phi_{beads} \\ \phi_{cup2} &= \phi_{bkg} + \phi_{straw} \\ \phi_{cup3} &= \phi_{bkg} \end{aligned} \tag{3.2.4}$$

where ϕ_{bkg} was the background phase induced from eddy currents and the geometry of the cup itself. The induced phase ϕ_{straw} was due to the susceptibility difference between the straw wall and doped gel ($\Delta\chi_{straw-Gd}$). Similarly, ϕ_{beads} was the induced phase due to the susceptibility difference between each bead and the doped gel ($\Delta\chi_{bead-Gd}$).

The goals in this subsection were to quantify the correct phase inside the straw containing beads ($\phi_{in,beads}$) and to measure the bulk susceptibility of the beads relative to that of gel doped with Gd-DTPA, $\lambda_{beads}\Delta\chi_{bead-Gd}$, where λ_{beads} was the volume fraction of the beads. Ideally we could subtract ϕ_{cup2} from ϕ_{cup1} through a complex division, leaving only ϕ_{beads} and $\phi_{in,beads}$ in phase images. However, as the straw positions in Cups 1 and 2 did not match perfectly, the first required

step was to remove ϕ_{bkg} from both ϕ_{cup1} and ϕ_{cup2} through complex divisions with ϕ_{cup3}. After each complex division, a constant background phase still remained in each set of phase images, ϕ_{cup1} and ϕ_{cup2}. This constant phase needed to be estimated and removed in order to obtain accurate measurements of ϕ_{beads} and $\phi_{in,beads}$. To achieve this, we had to first roughly estimate and remove ϕ_{straw} and $\phi_{straw}+\phi_{beads}$ from ϕ_{cup1} and ϕ_{cup2}, respectively, with the remaining phase assumed to be a constant. As the CISSCO method was insensitive to the additional constant background phase for a cylinder perpendicular to B_0 [5, 15], we used CISSCO to quantify the effective magnetic moments and centers of the straws (with and without beads) and used these information to forward simulate ϕ_{straw} and $\phi_{straw}+\phi_{beads}$. We then removed them from ϕ_{cup2} and ϕ_{cup1} through another complex divisions, respectively, and estimated the constant background phase in each set of images. After we removed the estimated constant background phase values from ϕ_{cup2} and ϕ_{cup1}, this resulted in more accurate phase distributions inside and outside the straws. From here, the effective magnetic moments of both straws (from Cups 1 and 2) were re-quantified. The difference of these two effective magnetic moments led to the effective magnetic moment of the cylindrical gel containing beads. Given the known inner radius of the straw, this effective magnetic moment allowed us to directly calculate $\lambda_{beads}\Delta\chi_{bead-Gd}$. On the other hand, as the straw had no effect on the phase inside, after removing the constant background phase, we directly measured the remaining phase inside the straw containing beads ($\phi_{in,beads}$) from ϕ_{cup1}. For the straw parallel to B_0, as $\phi_{straw}=\phi_{beads}=0$ outside the straw, the constant background phase was

directly measured and removed from complex divided images between Cups 1 and 3, i.e., $-i\ln(\exp(i\phi_{cup1})/\exp(i\phi_{cup3}))$. This whole procedure was performed on the central slice of the straw for each echo time and the results were averaged over all echo times.

Given the low number of particles per voxel, it was important to average the phase over many voxels inside the straw for analysis. The same process to analyze the nanoparticle magnitude and phase data was used here, by averaging sixteen pixels from each slice over 9 central slices inside the straw. The R_2^* were determined from the first three echo time of the bead data.

3.2.4.3 Simulated Data

Simulated images were analyzed in the same way as done for the above experimental data, except that sixteen pixels from each slice of only the central six slices were averaged. This choice was because the simulated images were more accurate for pixels closer to the central slice. Bulk susceptibilities, phase values inside straws, and relaxation rates were all compared between simulations and experiments.

3.3 Results

Bulk susceptibilities quantified from CISSCO are given in Table 3.1. These results between experiments and simulations are in very good agreements.

Figures 3.4 and 3.5 show mean phase values inside straws from the experiments, simulations, and theoretical values from Eqn. 3.2.2 and Eqn. 3.2.3. Data points from images at long echo times with an SNR less than 3:1 are not shown. Error bars in these plots represent the standard error of the mean. In general,

simulated results from randomly distributed particles agree with experimental results and the formula given by Eqn. 3.2.3, except for the nanoparticle solution perpendicular to the field with a bulk susceptibility of 0.29 ppm (Fig. 3.4a) or for long echo times (Figs. 3.4 and 3.5). As we see from simulated results shown in Fig. 3.6, different particle arrangements inside a long cylinder can lead to non-linear phase dependence of echo time. This nonlinear behavior appears more obvious when we further restrict the particle's freedom of movement toward a lattice arrangement. In the case shown in Fig. 3.4a, simulated results with the quasi-random arrangement using a cubic sub-volume of 26^3 grid points agree better with experimental data.

As demonstrated from three different voxels in Fig. 3.7, it is clear that Gibb's ringing over the cross sectional plane of a simulated cylinder shows a large effect from voxel to voxel. Thus, the simulated data must be averaged over a sufficient number of symmetric voxels inside a narrow cylinder.

Table 3.2 shows R_2^* quantified from experiments and R_2' from corresponding simulations with random particle arrangements. The R_2^* values from nanoparticle experiments are in good agreements with original results from [22]. The R_2' values quantified from simulations agree with the theoretical $R_2' = 0.4\gamma B_0|\Delta\chi'|$ [2] within uncertainties, although each uncertainty of R_2' is quite large even when no thermal noise is included in simulations. Those R_2' values from simulations also agree with experimental data, except for the highest bulk susceptibility of the nanoparticle solution. The disagreement in that case has been explained in [22]. There appears to be no dependence of cylinder orientation on R_2^* from

experiments or R_2' from simulations. In the quasi-random and lattice arrangements of particles in simulations, it is seen that R_2' increases as the particles become more ordered, while the quantified bulk susceptibility from phase outside the cylinder is unaffected (Table 3.3). The former statement is in agreement with results from [14]. When the particles are completely random, R_2' agrees with the predictions from [2]. See Table 3.2 and Table 3.3.

Based on the quantified bulk susceptibility and known volume fraction, we estimated a susceptibility of roughly -6.5 ppm for our beads relative to the doped gel, while its theoretical value was -9.66 ppm. From the effective magnetic moment quantified from the straw wall relative to Gd-DTPA doped gel (i.e., Cup 2), the estimated $|\Delta\chi_{straw-Gd}|$ was 9.3 ppm, which agreed with the theoretical molar susceptibility from [31]. Thus, our numbers here showed that the susceptibility of our beads was not -0.26 ppm relative to that of water, as given by [32]. In fact, the mass density of polystyrene beads should be about 1.05 g/cm^3, but we have found that the mass density of our beads is at least 1.2 g/cm^3, which indicates that our beads are not made of pure polystyrene.

3.4 Discussion

Our experimental and simulated results from a simple system disagree with current theories applicable to the static dephasing regime. Yablonskiy and Haacke [2] have considered spherical magnetic particles randomly distributed in a large space without a defined geometry. In other words, as long as spherical magnetic particles are randomly distributed in a large space with a low volume fraction, their theoretical formula, which gives a constant frequency shift shown in our

Eqn. 3.2.3, is what we should expect when the factor $\delta\omega_s \cdot t$, which is equal to the absolute phase value on the equator of the spherical particle, is much larger than 1. However, it is in this range that we observe deviations from their prediction, in both experiments and simulations.

The implication of this work will be applicable to the subcortical gray matter in the basal ganglia, whose major susceptibility source is ferritin. As far as the subcortical gray matter is considered, Eqn. 5 of [7] suggests that no (or little) additional phase shift would be observed, after the Lorentz sphere correction (Eqn. 2 of [7]). In other words, under the static dephasing regime, Yablonskiy and Haacke [2] would suggest an additional phase shift in the subcortical gray matter, but He and Yablonskiy [7] would not. However, Figs. 3.4 and 3.5 show additional phase shifts from randomly distributed magnetic spheres inside large cylinders, and those additional phase shifts do not completely agree with any theory. We also note that those additional phase shifts at each echo time seem to be independent of the orientation of the cylinders.

The phase shift as a function of echo time due to the presence of discrete particles is nonlinear. In addition, different arrangements of particles can lead to different phase values inside an object of interest. The recent work by [13] has shown from simulations that the constant frequency shift from [2] is valid in the static dephasing regime, as long as the volume fraction of spherical particles is less than 20%. However, this statement is not the complete story, given that all volume fractions of simulated spheres in our work are less than 20%. Looking closely, each of our simulated results at the longest echo time from randomly

distributed particles shows a deviation from Eqn. 12 in [2]. At those echo times, the factor $\delta\omega_s \cdot t$ ranges from 17 to 27. From a theoretical point of view, the larger the factor $\delta\omega_s \cdot t$ is, the better the agreement between simulations and predicted shift should be. However that is not the case here. When we simulate phase values from echo times between 15 ms and 30 ms for the 1.11 ppm case, those results become nonlinear and do not agree with Eqn. 3.2.3 at all. Furthermore, when we simulated particles randomly distributed in a cube as described in [14], the additional phase shift was completely different from Eqn. 12 in [2]. This can already be seen from our previous work in [11].

Our results may explain the additional frequency shifts shown by [33, 34] in the subcortical gray matter. In past work such as [7], microstructures such as cylinders representing axons in the white matter lead to nonlinear phase shifts. The recent trend is to use Generalized Lorentzian approach [7], susceptibility anisotropy [35, 36], or ellipsoidal microstructures [37, 38] to explain the phenomena. The focus has been white matter, not gray matter. Rudko et al. [39] has shown additional phase shifts from the cortical gray matter, but that situation mimics myelin in the white matter. Schweser and Zivadinov [34] recently has also stated and shown that additional frequency shifts appear in the subcortical gray matter, although they only suggest the possibility of chemical shifts and fast exchange processes as the sources. They then go on to refer to such shifts as “non-susceptibility contributions”, which were actually found to be larger in the subcortical gray matter than in the white matter. A similar work by [33] had considered those additional frequency shifts only as chemical shifts. Thus, with

a relatively small volume fraction of magnetic spherical particles, no one else has expected to see additional nonlinear phase shifts from spherical particles, which only have a constant susceptibility value. Those "non-susceptibility" phase shifts determined from [34] or "chemical shifts" from [33] may still be from the susceptibility effect, as we have demonstrated here. Furthermore, the consequence of our work affects QSM methods, especially in the subcortical gray matter.

The phase shifts we observed demonstrate that our experiments are not in the fast diffusion regime. For determining whether a particle is in the static dephasing regime, we have considered two inequality formulas each given in [2, 40]. In either formula, our bead experiments are in the static dephasing regime. On the other hand, as nanoparticles typically are smaller than 50 nm in diameter, with a field strength of 3 T, a diffusion constant of 2.5 μm^2/ms, and an echo time of 10 ms, either formula would predict the fast diffusion regime for nanoparticle solutions. As a result, one would expect no additional phase shifts inside the straws. This contradicts to our experimental results. This mismatch may be explained by nanoparticle clustering. An effective nanoparticle size of around 120 nm [40] (or 270 nm [2]) in diameter would push the signals into the static dephasing regime. Additional phase shifts observed from some ferritin solutions in [22] also indicate clustering of ferritin to a diameter of at least 0.5 μm. However, some diffusion effects apparently exist with the static dephasing effect, as those observed phase shifts from ferritin solutions are much smaller than values estimated from Eqn. 3.2.1 or our simulated results. This is also supported by the fact that the R_2^* measured from those ferritin solutions are much smaller

than the R_2' estimated from simulations [22], as the diffusion effect will reduce R_2^* [16, 17]. Furthermore, increased R_2 observed in tissues which contain ferritin compared to ferritin solutions has been attributed to clustering in tissues [41]. Histological staining for iron in the substantia nigra also indicates clustering of ferritin with diameters on the order of 10 μm [42] which would put it well into the static dephasing regime. All these results suggest applications of QSM to iron quantification in the gray matter structure will likely lead to erroneous results, as QSM utilizes phase data both inside and outside objects. On the other hand, if only the phase outside an object is used for quantification, without being affected by the factors studied here, the magnetic moment of the object can be accurately quantified [43] and the bulk susceptibility of the object may also be accurately quantified with the known volume of the object.

The fact that nonlinear additional phase shifts varying over echo time can arise from only spherical particles with a constant susceptibility emphasizes the need for knowing details of microstructures. This fact also makes it difficult to establish a general theory, especially in the static dephasing regime that is considered in this work. Before introducing a new theory such as [7] or susceptibility anisotropy of a tissue or object [35, 36], fields induced from discrete magnetic inclusions should be added first in the fashion of classical physics for the consideration of the additional phase shifts in tissues or objects containing microstructures.

3.5 Conclusion

We have shown that MRI phase signals inside long cylinders containing spherical particles with a constant susceptibility can vary nonlinearly with echo time especially when the number of particles per voxel is low or when Gibb's ringing is heavily affecting the phase inside the objects. This observation, based on the principles of physics and MRI, is important to be taken into consideration, before other theories or susceptibility anisotropy is introduced for the revision of QSM. While only a simple model of discrete spheres within a cylinder is presented, it should be easy to see how these results could be extended to at least the subcortical gray matter which has more complicated geometries. The additional phase shifts, whether nonlinear or not, can affect in vivo QSM results. In addition, the fairly large uncertainties of R_2' from simulations may also appear in the quantification of human data as well. On the other hand, phase distributions outside an object containing discrete spherical magnetic particles such as ferritin can be a more reliable source for accurate quantification of its bulk susceptibility.

Table 3.1: Bulk susceptibility $\Delta\chi'$ (in ppm) of each experimental and simulated cylinder. These values are calculated from the known cylinder (or straw) radius and the magnetic moments further quantified from the CISSCO method.

Fe_3O_4	experiment	1.11 ± 0.02	0.56 ± 0.01	0.29 ± 0.03
	simulations	1.08 ± 0.02	0.54 ± 0.01	0.28 ± 0.03
polystyrene beads	experiment	-0.24 ± 0.03		
	simulations	-0.24 ± 0.01		

Table 3.2: R_2^* and R_2' (in units of Hz) of experimental and simulated data, respectively. The theoretical values calculated for the static dephasing regime are also included. For Fe_3O_4 nanoparticles, the values in the displayed columns from left to right correspond to highest bulk susceptibility to lowest.

Fe_3O_4	experiment	parallel	180 ± 42	135 ± 29	73 ± 13
		perpendicular	201 ± 45	138 ± 26	74 ± 12
	simulation	parallel	318 ± 39	163 ± 14	90 ± 6
		perpendicular	317 ± 39	162 ± 21	85 ± 7
	theory	N/A	343	173	90
polystyrene beads	experiment	parallel	54 ± 36		
		perpendicular	57 ± 18		
	simulation	parallel	70 ± 10		
		perpendicular	71 ± 11		
	theory	N/A	74		

Table 3.3: Quantified $\Delta\chi'$ and R_2' from simulations using different particle arrangements. The more restricted arrangement of particles becomes, the larger R_2' becomes, while the quantified bulk susceptibility $\Delta\chi'$ from phase outside the cylinder is barely affected. This fact demonstrates the reliability of bulk susceptibility measurement from phase outside an object.

arrangement	sub-volume size	$\Delta\chi'$ (ppm)	R_2' (Hz)
random	N/A	$-0.24\pm$0.01	71$\pm$11
quasi-random	26^3	$-0.24\pm$0.01	87$\pm$12
quasi-random	14^3	$-0.24\pm$0.01	118$\pm$17
quasi-random	8^3	$-0.25\pm$0.01	135$\pm$19

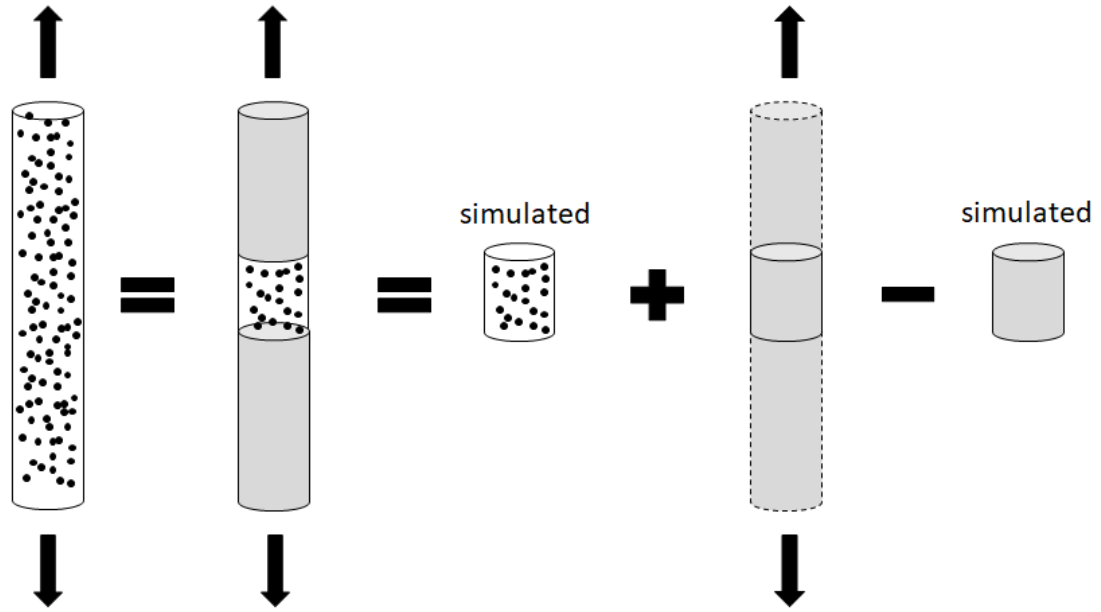

Figure 3.1: A graphical illustration of the first modification made to our simulations. Regions far from the center of our finite cylinder can be treated as continuous mediums. The cylinder is modeled within a rectangular FOV, where all the fields and MRI signals are calculated for each grid point. This modification reduces the memory required for simulations as we only need to model the central finite section of an infinitely long cylinder.

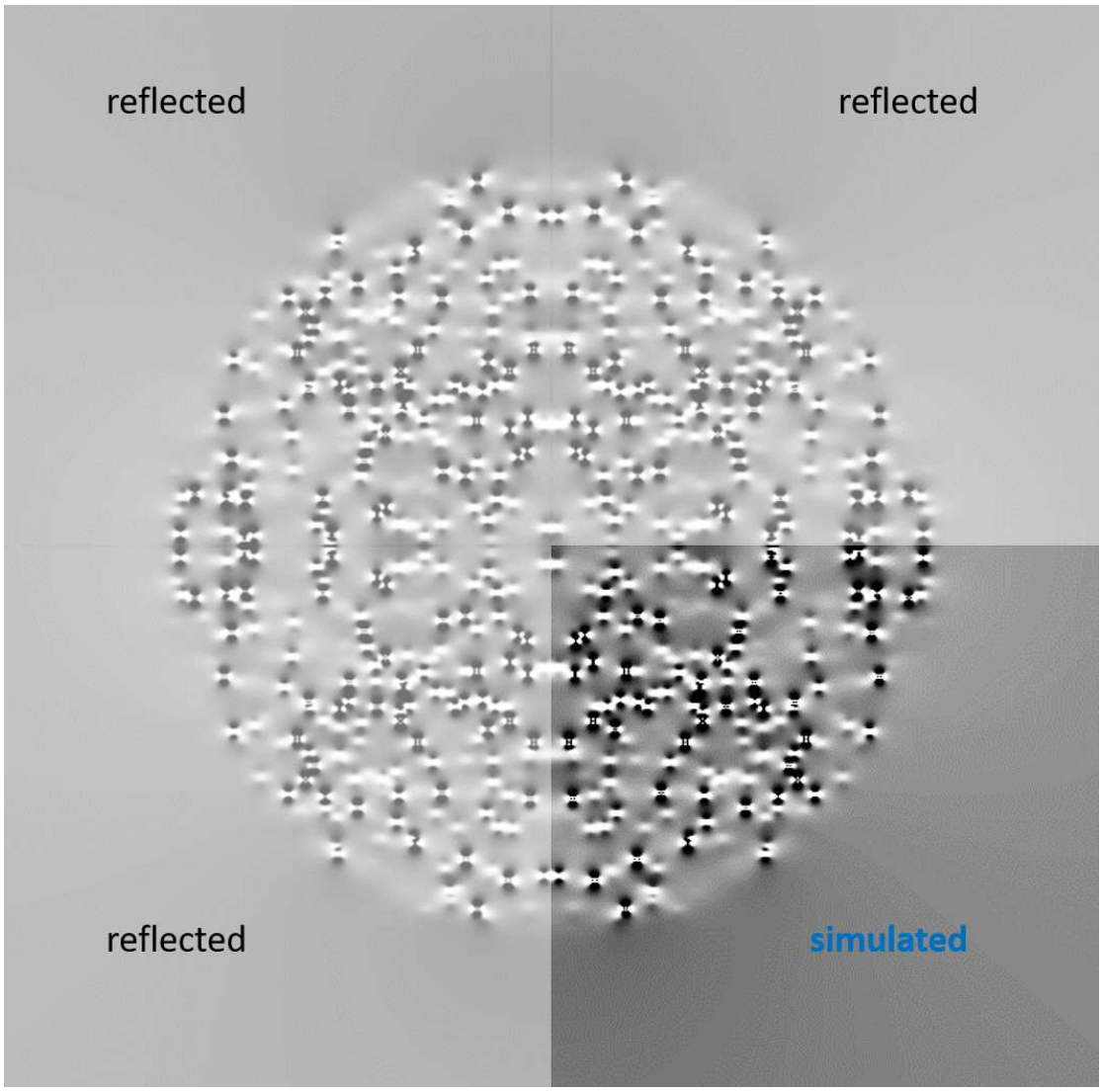

Figure 3.2: A high-resolution cross-sectional phase image of the simulated cylinder containing randomly distributed spherical particles. This demonstrates the second modification made to our simulations. Only one octant of the cylinder is actually simulated and all other octants are later reflected in the low resolution. This modification reduces the memory and time required for simulations by a factor of 16.

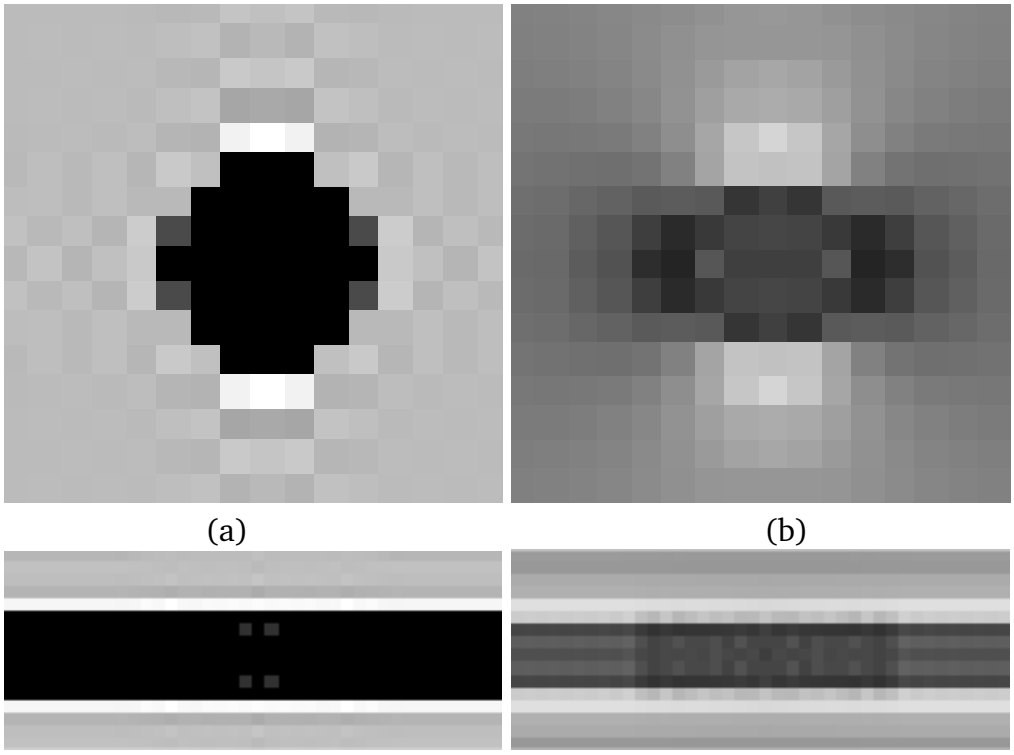

Figure 3.3: Simulated images with a bulk susceptibility of 0.29 ppm intended for nanoparticles in an infinitely long cylinder perpendicular to the main field. (a) Magnitude and (b) phase image display the middle cross section (i.e., central slice) of the cylinder. (c) Magnitude and (d) phase image display the cross section parallel to the cylinder axis. The difference between the central finite section where individual particles are simulated versus the sections which are treated as continuous above and below the central section can be seen in (d).

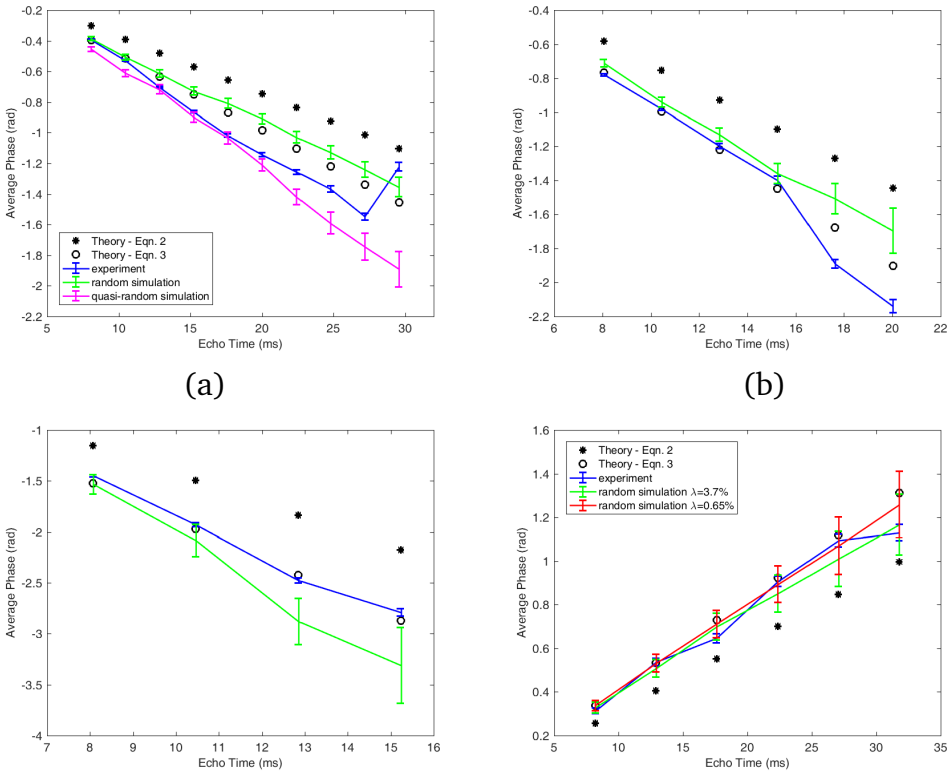

Figure 3.4: Experimental and simulated results, as well as two theoretical predictions, of phase inside cylinders perpendicular to the field are shown for bulk susceptibilities of (a) 0.29 ppm, (b) 0.56 ppm, (c) 1.11 ppm, and (d) -0.24 ppm. Asterisk markers represent the phase calculated from Eqn. 3.2.2. Open circle markers represent phase calculated from Eqn. 3.2.3. The blue lines represent the experimental data and the green lines represent simulated results using random particle arrangements. In (a), a quasi-random simulation is plotted in magenta with each particle allowed to move within a sub-volume of 26^3 grid points. These results seem to agree with the experimental data better. In (d), the green and the red line are from particle volume fractions of 3.7% and 0.65%, respectively, with the same bulk susceptibility. While both results agree well with the experimental data, the outcome from the volume fraction of 3.7% agrees better with the experimental data especially at the last echo time.

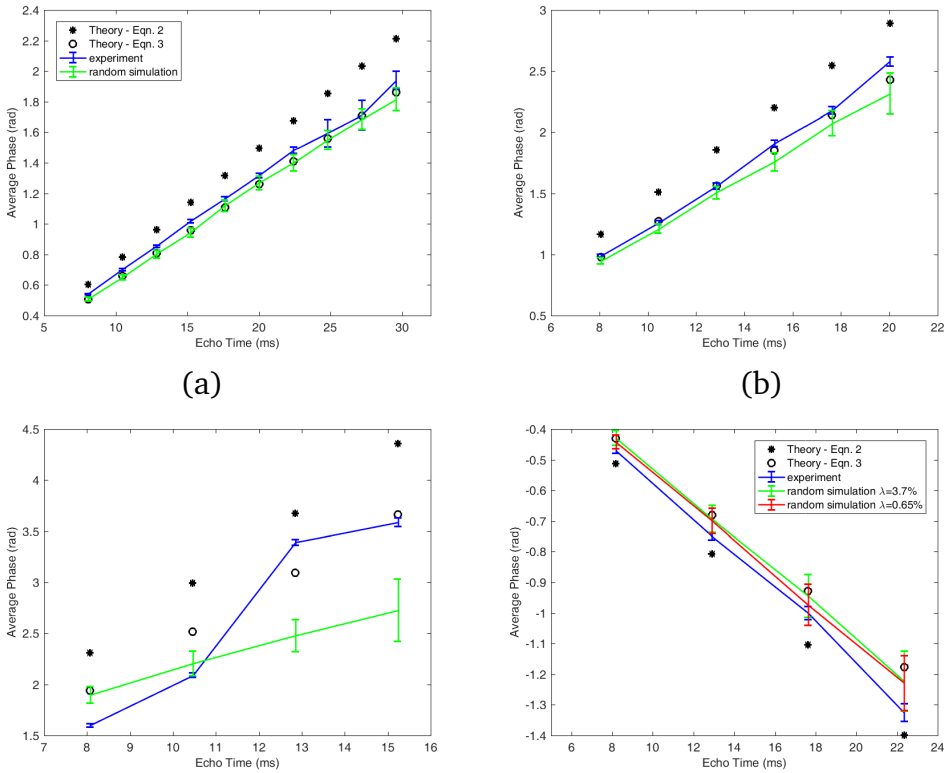

Figure 3.5: Experimental and simulated results, as well as two theoretical predictions, of phase inside cylinders parallel to the field are shown for bulk susceptibilities of (a) 0.29 ppm, (b) 0.56 ppm, (c) 1.11 ppm, and (d) -0.24 ppm. Meanings of the symbols and curves have been explained in the caption of Fig. 3.4.

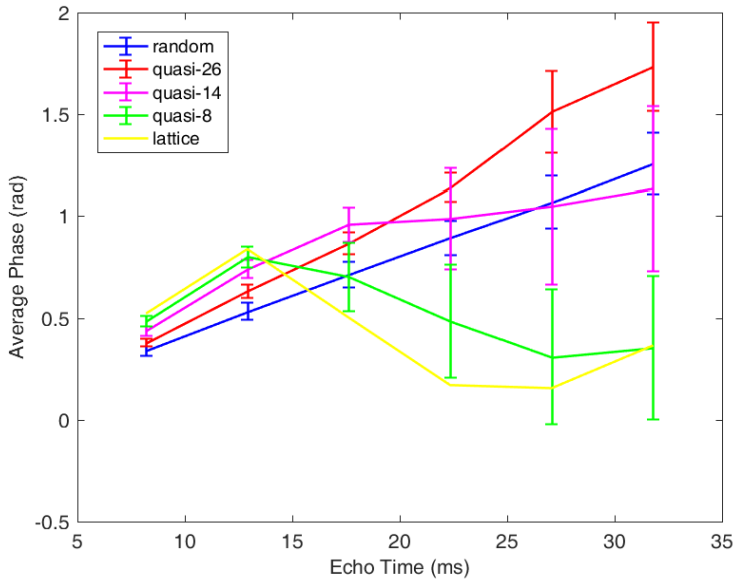

Figure 3.6: Simulated phase values inside a cylinder perpendicular to the main field from different particle arrangements for a bulk susceptibility of -0.24 ppm are shown as a function of echo time. Random particle arrangements, lattice, and quasi-random arrangements with each particle restricted within sub-volumes of 26^3, 14^3, and 8^3 grid points are simulated. Restricting particle arrangements leads to nonlinear phase dependence of echo time.

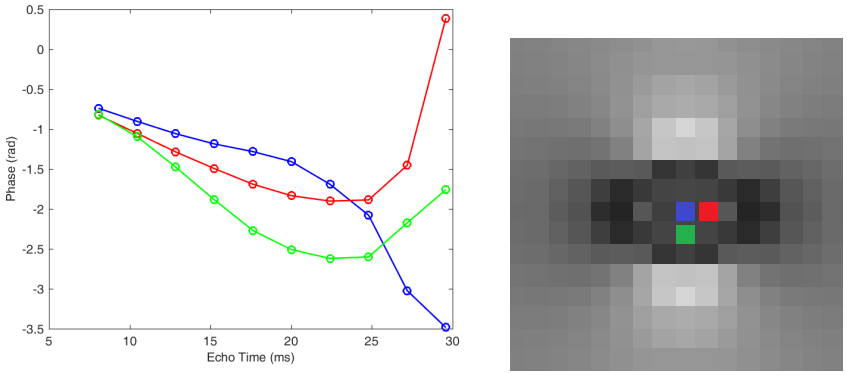

(a) (b)

Figure 3.7: (a) Phase values from three individual voxels inside an infinitely long cylinder perpendicular to the main field simulated for nanoparticles with a bulk susceptibility of 0.56 ppm. (b) The cross sectional plane of the simulated cylinder. Each color curve in (a) corresponds to the same color voxel in (b).

CHAPTER 4 QUANTIFICATIONS OF IN VIVO LABELED STEM CELLS BASED ON MEASUREMENTS OF MAGNETIC MOMENTS

4.1 Introduction

Cell-based treatments have shown promising results in neurological diseases in laboratory animals [44, 45] and patients [46, 47]. Therapeutic benefit using neural progenitor cells (NPCs) depends on the migration and localizations of the grafted cells within the target tissue [48–50]. Magnetic resonance imaging (MRI) has demonstrated its ability in monitoring cell migration and distributions using dextran-coated superparamagnetic iron oxide (SPIO) nanoparticles with transfer agents [51–62]. Quantification of SPIO tagged cells may open the door to more detailed studies on their behaviors after SPIO are administered into the body, yet quantification of *in vivo* labeled cells remains a challenge. Assessment of iron (e.g., brain iron) has typically involved the measurement of proton transverse relaxation rate, R_2 [63–68]. Several studies have observed a relationship between R_2 (or R_2^*) and labeled cell concentration in vitro [69, 70] . However, the relationship between R_2 and labeled cell concentration is much more complicated *in vivo* and may involve diffusion [71]. Quantifications of labeled cell concentrations using R_2 and diffusion require the removal of background effects induced by neurological diseases [71].

Previously, Del Gratta et al. [72] had estimated numbers of cells *ex vivo* using a Superconducting Quantum Interference Device (SQUID) magnetometer. In this work, we propose to use the Complex Image Summation around a Spherical or Cylindrical Object (CISSCO) method [6] to quantify the magnetic moment of

SPIO nanoparticle tagged stem cells in a local cluster from MR images. In turn, we estimate the number of cells from each cluster. For the magnetic moment quantification of small objects, the CISSCO method has been tested and shown to provide good accuracy [6].

Magnetostatic theory governs that small magnetized objects, regardless of geometry, can be modeled as perfect spheres. The magnetic moment of an object can be expressed as the product of its mass magnetization and mass. Thus, given the known mass magnetization of iron nanoparticles and the quantified magnetic moment of the nanoparticle cluster, the mass of nanoparticles in a local cluster can be calculated. Further, if the cellular iron uptake is known, the mass of nanoparticles can be used to derive the number of cells. In order to apply the CISSCO method to *in vivo* images, we first simulate and study the effect of high-pass (HP) filters and systematic errors on magnetic moment quantifications. High-pass filtering [73] has been a relatively easy and effective method for eliminating background fields from phase images. Next, an improved version of the CISSCO method for *in vivo* applications is tested on simulations and then applied to six clusters of cells in several existing rat brain images.

4.2 Materials and Methods

4.2.1 Simulations

We simulated several spheres that represent cell clusters, which in reality contains numerous nanoparticles. Given various magnetic moments and radii of simulated spheres, each simulation was forward modeled on a 1024^3 matrix and cropped down to 32^3 in the spatial frequency domain. Detailed procedures were

given in [6]. For display purposes and analyses of HP filters, each of the 32 slices was zero-filled (zero phase value and a predefined constant magnitude intensity outside the 32×32 matrix) in image space to 256^2. A total of 15 spheres were simulated with targeted effective magnetic moments (p) of 8, 15, 20, 30, and 100 radian·pixel^3 and radii (a) of 1, 2, and 3 pixels in the 32^3 matrix. The effective magnetic moment of each simulated sphere from CISSCO has been defined as $p = 0.5\gamma\Delta\chi B_0 T_E V$, where $\gamma = 42.58$ MHz/T, B_0 is the main field, T_E is the echo time, $\Delta\chi$ is the susceptibility difference between the sphere and its surrounding, and V is the volume of the sphere. As $0.5\gamma\Delta\chi B_0 T_E$ is a product of 4 parameters and can be rewritten as p divided by a^3, it is more general to consider the radius and the effective magnetic moment for each simulation (rather than each individual parameter). This effective magnetic moment has a unit of radian·pixel^3 if the volume of the sphere is measured in terms of pixel^3 directly from images. In the case of nanoparticles in tissues, $\Delta\chi B_0 V$ can be approximated by $\mu_0\mu$ [74], where $\mu_0 = 4\pi \times 10^{-7}$ Wb/(A·m) and μ is the overall magnetic moment of nanoparticles within a cluster in a tissue and has a unit of A·m^2. For simplicity, p refers to the "magnetic moment" hereafter. No Gaussian noise was added to any of the simulations in order to examine the effect of the HP filter and its systematic errors. All magnetic moment quantifications from CISSCO were performed using codes developed in Visual C++.

4.2.2 CISSCO Procedure

The procedure of magnetic moment quantifications using CISSCO has been given in [6]. Briefly, each voxel is first interpolated into 1000 subvoxels for

subsequent steps. Second, the center of an object of interest is identified by minimizing the real part of the overall signal summed within an arbitrary sphere chosen by the user. Third, the magnetic moment p of the object is solved from the following equation

$$Re(S_1 - S_2)Re(f_{23}(p)) = Re(S_2 - S_3)Re(f_{12}(p)) \tag{4.2.1}$$

where S_1, S_2, and S_3 are the complex sums within three concentric pseudo spheres with radii R_1, R_2, and R_3 defined by the user, and $f_{12}(p)$ and $f_{23}(p)$ are analytical functions given by equations 6, 9, and 10 of [6] and shown below. They represent the normalized theoretical sums of complex signals within pseudo shells defined by the three radii. Note that $R_1 > R_2 > R_3$.

$$\begin{aligned} f_{ij}(p) \equiv R_i^3 \int_1^{\frac{R_i^3}{R_j^3}} \frac{dx}{x^2} \left(2e^{ix\frac{p}{R_i^3}} + e^{-2ix\frac{p}{R_i^3}} \right) \\ + \int_{-1}^{2} \frac{dx}{x^2} [2 - (2-x)\sqrt{1+x}] \left(R_i^3 e^{-ix\frac{p}{R_i^3}} - R_j^3 e^{-ix\frac{p}{R_j^3}} \right) \end{aligned} \tag{4.2.2}$$

4.2.3 Improved CISSCO Approach

As an *in vivo* object can be subject to local background magnetic fields induced from other nearby tissues, it is important to correct this problem in the CISSCO method. Given the fact that we are interested in small objects, we may approximate those local background fields as a constant local field around each object. This local constant background field may affect the determination of the object center in CISSCO as well as the quantification of the magnetic moment. To study the effect analytically, we have added a constant background phase ϕ_{bkg}

to signal S defined in [6]. The signal becomes $Se^{i\phi_{bkg}}$. Regardless of the value of ϕ_{bkg}, it should be clear from [6] that first derivatives and cross terms of second derivatives of $Se^{i\phi_{bkg}}$ are all zero, when the center of the object is identified at $r_0 = 0$. The remaining second derivatives can be written down according to Eq. 27 of [6].

$$
\begin{aligned}
\left.\frac{\partial^2 Se^{i\phi_{bkg}}}{\partial x_0^2}\right|_{r_0=0} &= 2\pi\rho_0 a e^{i\phi_{bkg}}\left[\int_0^1 dx\,(3x^2-1)f_a\right. \\
&\quad -3\phi_a^{1/3}\int_{\phi_R}^{\phi_a}\phi^{2/3}d\phi\int_0^1 dx(5x^2-1)^2(1-x^2)f_\phi \\
&\quad +3i\phi_a\int_0^1 dx\,(7x^2-1)(1-x^2)f_a \\
&\quad \left.+i\phi_a^{1/3}\int_{\phi_R}^{\phi_a}\frac{d\phi}{\phi^{1/3}}\int_0^1 dx(35x^4-30x^2+3)f_\phi\right] \\
\left.\frac{\partial^2 Se^{i\phi_{bkg}}}{\partial y_0^2}\right|_{r_0=0} &= \left.\frac{\partial^2 Se^{i\phi_{bkg}}}{\partial x_0^2}\right|_{r_0=0} \\
\left.\frac{\partial^2 Se^{i\phi_{bkg}}}{\partial z_0^2}\right|_{r_0=0} &= -4\pi\rho_0 a e^{i\phi_{bkg}}\left[\int_0^1 dx\,(3x^2-1)f_a\right. \\
&\quad +3\phi_a^{1/3}\int_{\phi_R}^{\phi_a}\phi^{2/3}d\phi\int_0^1 dx(3-5x^2)^2x^2f_\phi \\
&\quad +3i\phi_a\int_0^1 dx\,(5-7x^2)x^2f_a \\
&\quad \left.+i\phi_a^{1/3}\int_{\phi_R}^{\phi_a}\frac{d\phi}{\phi^{1/3}}\int_0^1 dx(35x^4-30x^2+3)f_\phi\right] \qquad (4.2.3)
\end{aligned}
$$

where ρ_0 is the spin density of the tissue around the object, $f_a \equiv \exp\{-i\phi_a(3x^2-1)\}$, $f_\phi \equiv \exp\{-i\phi(3x^2-1)\}$, $\phi_a \equiv p/a^3$, $\phi_R \equiv p/R^3$, and R is the radius of the sphere that a user chooses to identify the center of the object. The goal is to determine, under what ϕ_{bkg}, ϕ_a, and ϕ_R values that real parts of all three second derivatives are positive. We consider ϕ_{bkg} ranging from -1.5 radians to $+1$ radian in an increment of 0.1 radian for a series of numerical evaluations. For each value of ϕ_{bkg}, we have varied ϕ_a from 0.1 to 3π radians and ϕ_R from 0.1 to

π radians in order to examine the signs of those second derivatives. As ϕ_R indirectly defines the radius of the sphere that the user chooses to find the center of the object, this gives a scale invariant variable to use, rather than to use the magnetic moment p in these calculations. The range of ϕ_R under consideration is always between 0 and π [6]. If ϕ_a is larger than 3π, given the dephasing effect around the object of interest, in order to identify its center, the object can be substituted by a larger object (but the same magnetic moment) such that its ϕ_a is less than 3π.

Next, in order to eliminate this constant field term when we solve for the magnetic moment, based on the original derivations of the CISSCO method in [6], we can consider the magnitude squared of the complex signals rather than their real parts. We thus have

$$|S_1 - S_2|^2 |f_{23}(p)|^2 = |S_2 - S_3|^2 |f_{12}(p)|^2 \tag{4.2.4}$$

It should be clear from Eq. 4.2.4 that the local constant phase term will not affect the quantification of the magnetic moment. To verify this, we will add a constant background phase ranging from -1 to 1 radian in increments of 0.1 radian, to a simulated sphere with a radius of 1 pixel and a magnetic moment of 20 radian·pixel^3. Each case will be quantified by both the original CISSCO method and the improved method. This alternate approach also requires rederiving the uncertainty of the quantified magnetic moment, including both the Gaussian noise and systematic error. This has been accomplished using a stan-

dard error propagation approach (See 4.6).

4.2.4 HP Filter

It was known that HP filters could affect phase values from large objects but it was not clear how HP filters could affect the magnetic moment quantification from CISSCO. Thus, high-pass filters with sizes of 16×16, 32×32, and 64×64, and with an additional Hanning filter multiplied to each HP filter in k-space were applied to each slice of the simulated data. The magnetic moment of each simulated sphere, before and after the applications of the HP filters, was quantified using CISSCO. This was to evaluate systematic errors purely from HP filters, rather than from Gibbs ringing or the partial volume effect. The radii of the three pseudo spheres used in CISSCO were chosen at least 0.5 pixel away from the surface of each spherical object and at least one pixel apart between any two pseudo spheres [6].

4.2.5 In Vivo Data and Analyses

We applied a 32×32 HP filter to four sets of archived 3D gradient echo rat images acquired in 2008 based on a stroke model performed in [71]. Neural progenitor cells were labeled using a Ferumoxide-Sulfate solution and were injected into those rat brains. Six isolated nanoparticle clusters from the four datasets were quantified with the CISSCO method. Two example clusters are shown in Fig. 4.1. The imaging parameters were $T_E = 10\,\text{ms}$, $T_R = 30\,\text{ms}$, $B_0 = 7\,\text{T}$, in-plane field of view = $32\,\text{mm} \times 32\,\text{mm}$, image resolution = $0.0625\,\text{mm} \times 0.125\,\text{mm} \times 0.25\,\text{mm}$, matrix size = $512 \times 256 \times 64$, slab thickness = 16 mm, flip angle = 25°, number of averages = 4, and scan time = 32

mins 46 sec. Original k-space data were used for image reconstructions. The reconstructed images were further interpolated to 0.125 mm isotropic resolution for CISSCO analyses. A T_2-weighted spin echo dataset with the same in-plane resolution was also obtained with the intent to estimate the volume of each cluster. However, clusters in spin echo images were unidentifiable. As the slice thickness of the spin echo images (0.8 mm) was about three times that of the gradient echo images, and spin echo images had sufficient signal-to-noise ratios in images, these facts implied that the overall volume of nanoparticles in each cluster was still much smaller than a voxel in gradient echo images.

The number of cells in each cluster was calculated from the following equation, with the result rounded to the nearest integer.

$$\begin{aligned}\text{Number of cells} = \mu(\text{A}\cdot\text{m}^2) &\times \frac{1}{\text{Ferumoxide mass magnetization}}\left(\frac{\text{kg}}{\text{A}\cdot\text{m}^2}\right) \\ &\times \frac{1}{\text{cell iron uptake}}\left(\frac{\text{cell}}{\text{kg Fe}}\right)\end{aligned} \tag{4.2.5}$$

where μ was calculated from the measured magnetic moment $p = 0.5\chi T_E \mu_0 \mu$. The saturation mass magnetization of Ferumoxide is $93.6 \pm 1.6\,\text{A}\cdot\text{m}^2/\text{kg}$ iron [75]. Values for cell iron uptake depend on the cell labeling agent and process, along with the type of cell being used. We chose 14.5 pg/cell from Panizzo et al. [76], as they used the same labeling agent, process, and cell type provided in [71].

4.3 Results

4.3.1 HP Filter

Simulations showed that, as the size of the applied HP filter increases, the quantified magnetic moment decreases (Fig. 4.2). The error is larger when either the magnetic moment or the radius of the simulated sphere is larger. The percentage differences in magnetic moment quantifications caused by the 32×32 HP filter can vary by a large range depending on the magnetic moment and radius of the sphere (Fig. 4.2d). For spheres with radii of 2 or 3 pixels, we observed a minimal value (i.e., error) in Fig. 4.2d, at the magnetic moment of about 30 radian·pixel^3. When the magnetic moment is smaller, the error increases. This is due to less than π radians of phase values outside the object such that other systematic errors affect the results more.

4.3.2 Improved CISSCO Approach

Figure 4.3 indicates the largest radius R within which complex signals can be summed over such that the center of an object of interest can be identified through Eq. 4.2.3. With a given local constant background phase, the radius R of the pseudo sphere needs to be chosen sufficiently large such that $|p/R^3|$ is less than the maximal $|\phi_R|$ value shown in Fig. 4.3.

Figure 4.4 shows results for quantification of a simulated sphere with a radius of 1 pixel and a true magnetic moment of 20 radian·pixel^3 over a range of background phases, using both the original and improved CISSCO method. When the original method was used, the quantified magnetic moment decreased from 24.3 radian·pixel^3 to 14.7 radian·pixel^3 as the background phase increased. On

the other hand, results from the improved method remained at 19.95 radian·pixel^3 for each background phase. It is clear that the improved approach is not at all susceptible to the added local constant background phase.

4.3.3 Number of Cells from In Vivo Data

Table 4.1 summarizes results from six stem cell clusters quantified from the CISSCO method. Each result was adjusted based on findings from the simulated HP filter results. As the uncertainty of mass magnetization of Ferumoxide is about 1.7% but the uncertainty of cell iron uptake is not known, the percentage error of each cell count is the sum of 1.7% and the percentage error estimated from CISSCO (third column in Table 4.1). All but one quantified results had less than 10% uncertainty. Table 4.1 also indicates that if one cell contains 14.5 pg of iron, then the quantified magnetic moment would be roughly 0.19 radian·pixel^3. Thus detecting one cell would require a higher image resolution than the current resolution. On the other hand, Heyn et al. [77] had a cellular iron uptake of 43.3 pg/cell and they were able to visually detect one cell. This 43.3 pg of iron per cell translates to a magnetic moment of roughly 0.56 radian·pixel^3, which is about the lower limit that our CISSCO method can quantify with an uncertainty of roughly 100%. In general, other studies [77–80] also have cellular iron uptakes at the same order of magnitude. Thus, their images can also be analyzed with our method.

4.4 Discussion

Our work has demonstrated that magnetic moments of isolated clusters of nanoparticle labeled cells can be accurately quantified from the applications of

the high pass filter and the improved CISSCO method. While our results were not validated by any histological method, several issues should be realized with performing such a validation. Although cell concentrations measured by MRI and histology were highly correlated, a histological approach has its own uncertainties. Each quantified number of labeled cells can vary by a factor of 4, indicated from private records in the work of [71]. Those uncertainties depend on cell size, cell division, labeled macrophage, cell death, image resolution, and also are based on the assumption that cells are uniformly distributed throughout the cluster. As a result, there is a strong need of a better method for the quantification of number of labeled cells, especially *in vivo*.

Although a larger magnetic moment will have a smaller uncertainty estimated from the CISSCO method, it will nonetheless have a larger error after the application of the HP filter. In addition, the larger the HP filter size is, the worse the underestimation of the result will be. As we are not able to spot each nanoparticle cluster from spin echo images, the overall volume of nanoparticles in a cluster has to be much smaller than a voxel. This is also consistent with small volumes estimated from quantified magnetic moments (Table 4.1) divided by a large magnetization of nanoparticles. These facts suggest that the 32×32 HP filter has little effects on our *in vivo* magnetic moment measurements. If we want to make some adjustments, we can use the curve in Fig. 4.2d, when the radius of the object a is 1 pixel.

While systematic error is ultimately unavoidable, it can be minimized by scanning with an isotropic image resolution. Although the actual geometry of each

cluster is not a perfect sphere, magnetostatic theory tells us that the magnetic moment of such a small object can be well approximated by that from a sphere. In order to improve the accuracy of each measurement, it is also important to re-measure the mass magnetization of nanoparticles and cell iron uptake used in a particular study. These two quantities can be measured in *ex vivo* settings.

Our results show that the improved CISSCO method is better than the original method, as constant background phase has no effect on quantifications. For use in center identification, our criteria on the radius R must be followed. Even though the magnetic moment p is not known beforehand, p/R^3 is the theoretical phase value on the equatorial plane around the spherical object and thus is roughly known from phase images. Because of that, and if the local constant background phase ϕ_{bkg} can also be estimated from phase images, then we can properly choose the radius R based on Fig. 4.3 for the determination of the object center. From a different consideration, if $|\phi_{bkg}|$ is relatively large, say more than 0.3 or 0.5 radian, we can consider subtracting a constant phase value around the object such that the remanent local background phase is within ± 0.3 or ± 0.5 radian. This will allow us to reduce the radius R, keep the pseudo sphere compact, and effectively identify the center of the object.

4.5 Conclusions

We have presented an improved method of magnetic moment quantification of labeled stem cell clusters from archived *in vivo* images. For this purpose, our simulations confirm that images filtered by a 32×32 high-pass filter only lead to slightly underestimated results. This improved CISSCO method is also insen-

sitive to the existence of local background field. Although we have not directly validated our method with histological results, past records indicate that histological results have large uncertainties. A better method of measuring number of labeled cells is needed. On the other hand, from the quantified magnetic moment, we can calculate the number of cells in each cluster to a reasonable accuracy. This offers a new potential for the measurement of the number of cells *in vivo*.

4.6 Appendix: Deriving Uncertainty of the Improved CISSCO Method

Error propagation is used to determine the uncertainty of the modified CISSCO method presented in this work. The equation used to solve for the magnetic moment is given by Eq. 4.2.4. The variation of Eq. 4.2.4 leads to

$$\frac{\delta p}{|p|} = \frac{1}{|D|}\sqrt{(\delta(|S_2 - S_3|^2))^2\frac{|f_{12}|^4}{p^2} + (\delta(|S_1 - S_2|^2))^2\frac{|f_{23}|^4}{p^2}} \tag{4.6.1}$$

where

$$D = \frac{\partial|f_{12}|^2}{\partial p}|S_2 - S_3|^2 - \frac{\partial|f_{23}|^2}{\partial p}|S_1 - S_2|^2 \tag{4.6.2}$$

Note that f_{ij} is given in Eq. 4.2.2 and the uncertainty of $|S_i - S_j|^2$ is defined as

$$\delta(|S_i - S_j|^2) = \sqrt{(\eta_{ij}|S_i - S_j|^2)^2 + \frac{16\pi}{3}\sigma^2(R_i^3 - R_j^3)\Delta x\Delta y\Delta z|S_i - S_j|^2} \tag{4.6.3}$$

where η_{ij} represents the systematic error of $|S_i - S_j|^2$ and σ^2 is the variance of the MR signal. We have assumed that the real part and imaginary part of

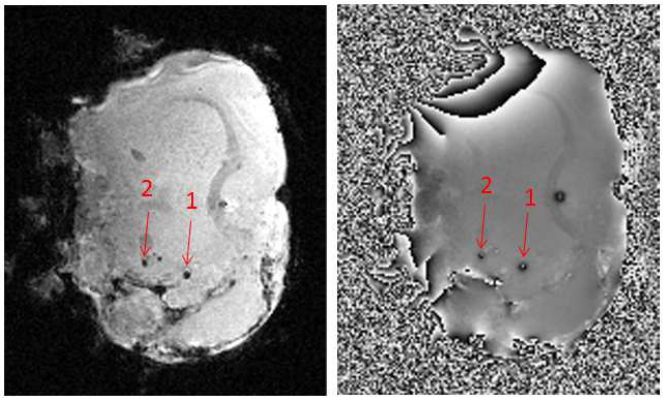

(a) (b)

Figure 4.1: Example (a) magnitude and (b) phase image of nanoparticle labeled cell clusters in a rat. Clusters that were quantified are identified by red arrows.

the MR image has the same variance, but their Gaussian noise is independent. Equation 4.6.3 is derived from the error propagation method. The systematic error η_{ij} is equal to the difference between the summed $|S_i - S_j|^2$ from images and the theoretical $|S_i - S_j|^2$ calculated from the integrals given in [6], divided by the theoretical $|S_i - S_j|^2$. The partial derivatives of $|f_{ij}|^2$ with respect to p are

$$\frac{\partial |f_{ij}(p)|^2}{\partial p} = 2Re(f_{ij}(p))\frac{\partial Re(f_{ij}(p))}{\partial p} + 2Im(f_{ij}(p))\frac{\partial Im(f_{ij}(p))}{\partial p} \tag{4.6.4}$$

The derivative of the real part of $f_{ij}(p)$ is given by Eq. 14 in [6] and the derivative of its imaginary part is

$$\begin{aligned}\frac{\partial Im(f_{ij}(p))}{\partial p} = 2\int_1^{\frac{R_i^3}{R_j^3}} \frac{dx}{x}\left[\cos\left(x\frac{p}{R_i^3}\right) - \cos\left(2x\frac{p}{R_i^3}\right)\right] \\ + \int_{-1}^{2} \frac{dx}{x}[2-(2-x)\sqrt{1+x}]\left[\cos\left(x\frac{p}{R_j^3}\right) - \cos\left(x\frac{p}{R_i^3}\right)\right]\end{aligned} \tag{4.6.5}$$

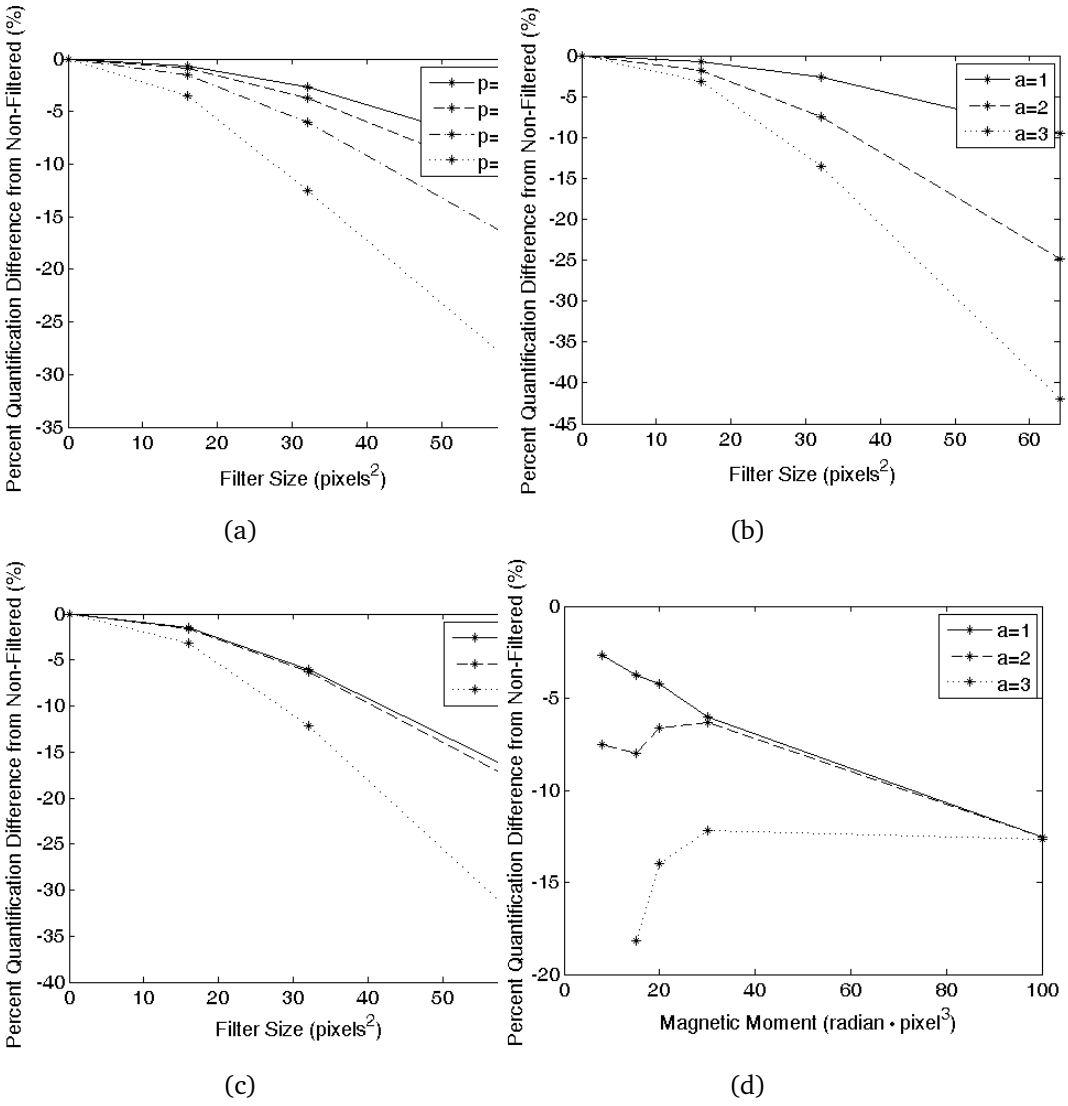

Figure 4.2: Percentage differences in magnetic moment quantifications as a function of filter sizes for simulated spheres with (a) a radius of 1 pixel, (b) a fixed magnetic moment of 8 radian·pixel^3, and (c) a fixed magnetic moment of 30 radian·pixel^3. (d) Percentage differences in magnetic moment quantifications as a function of magnetic moments. These results are from a fixed 32×32 HP filter but with different sphere sizes. Lines connecting data points do not have specific meanings.

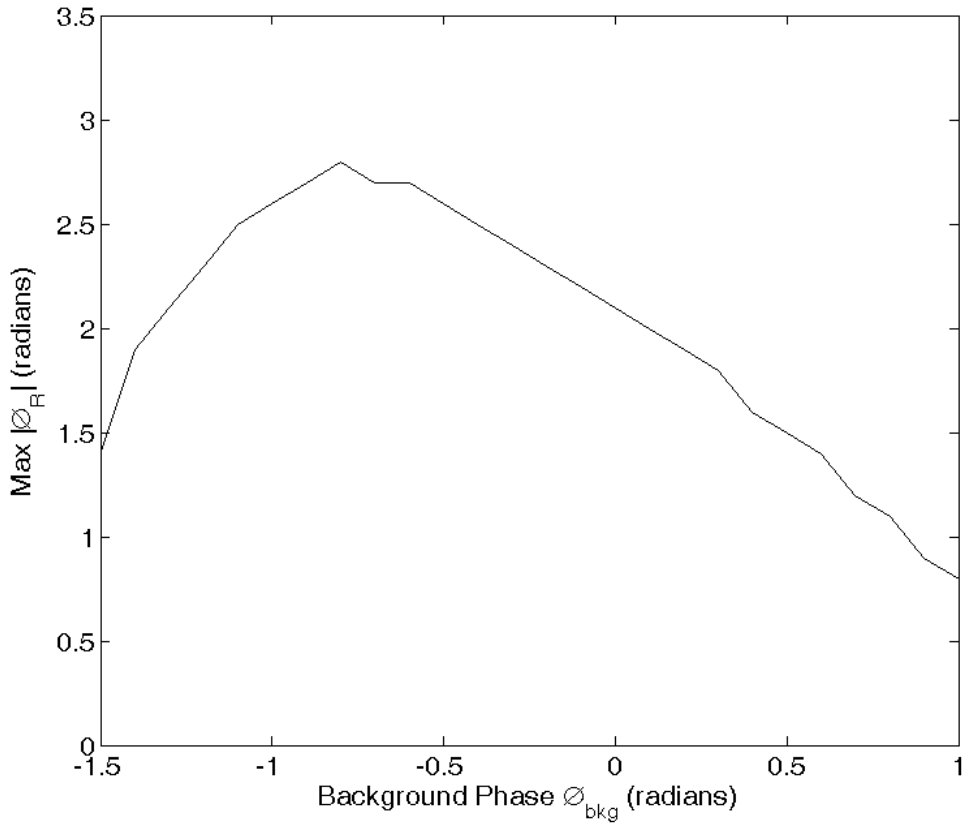

Figure 4.3: Maximal $|\phi_R|$ value as a function of the local constant background phase, ϕ_{bkg}. As ϕ_R indicates the phase values induced from the object on the equatorial plane, maximal $|\phi_R|$ associated with a given ϕ_{bkg} value implies how large the radius R should be chosen for the determination of the object center.

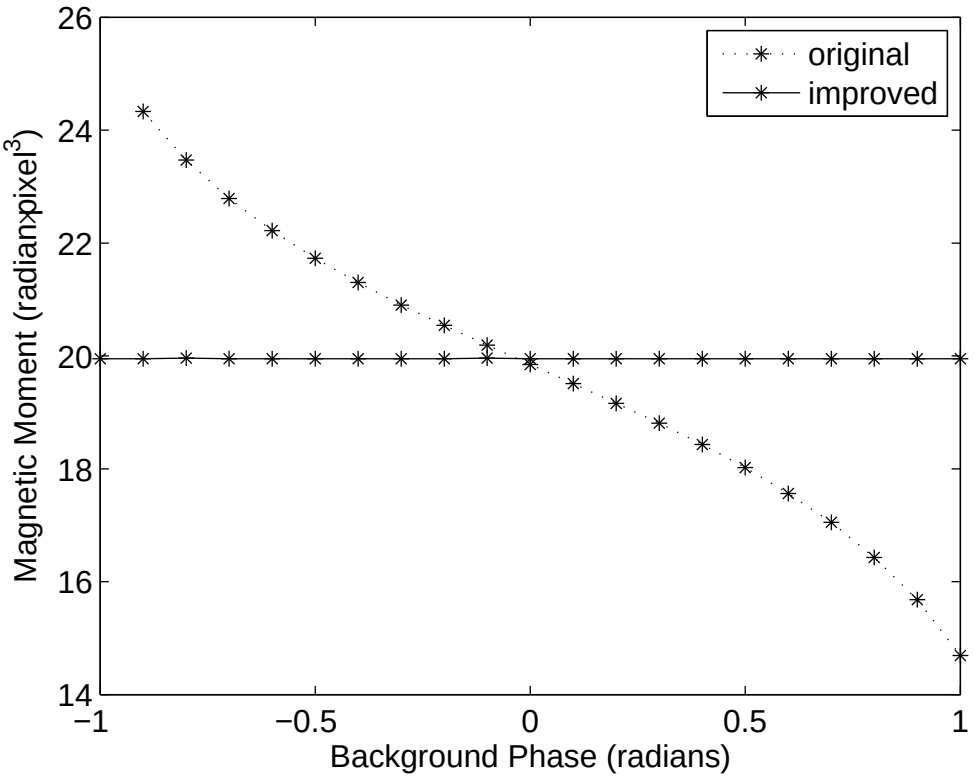

Figure 4.4: Quantified magnetic moments as a function of the local constant background phase using both the original (dotted line) and improved (solid line) CISSCO method. The improved method is completely unaffected by the addition of the background phase.

Cluster	p'_{HP}	$\delta p'/p'$ (%)	p'_{adj}	Cells	η_{12} (%)	η_{23} (%)
1	12.2	3.6	13.0	70	-0.5	0.3
2	5.38	2.4	5.72	31	-1.1	3.4
3	11.5	3.1	12.2	66	-0.5	-5.2
4	28.8	1.2	30.6	164	-1.4	2.4
5	7.66	8.8	8.15	44	-0.3	7.4
6	21.7	0.8	23.1	124	-1.6	0.9

Table 4.1: Quantified results of six nanoparticle clusters. The second column p'_{HP} represents each measured magnetic moment from CISSCO after images have been high-pass filtered. The unit of each measurement is radian·pixel^3. The third column lists the uncertainty (in percentage) of each quantified magnetic moment. The fourth column lists the HP filter corrected magnetic moment based on the value of p'_{HP} and the curve of $a = 1$ in Fig. 4.2d. The fifth column lists the number of cells calculated from the fourth column. The last two columns give the systematic errors from the magnitude squared procedure for each concentric shell used in the CISSCO method. Partial volume effects due to non-isotropic image resolutions are not included in these systematic errors.

CHAPTER 5 CONCLUSION AND FUTURE DIRECTIONS

In Chapter 2, guidelines of how to perform accurate simulations of mixtures of spherical particles in the static dephasing regime were determined. Some of the key findings here were that a particle radius of at least 4 grid points is needed to accurately construct the magnetic fields around the particle, that at least 1728 particles per voxel are needed to represent MRI signal behaviors of larger numbers, that having less particles in a voxel can lead to a high variance of phase values, that voxels surrounding a voxel of interest also need to be included in a given model, and how restricting the particles freedom of movement affects the magnitude and phase signal. These guidelines were then used to simulate large cylinders consisting of particles in Chapter 3 and the results were compared with experiments. Here it was shown how restricting particle freedom of movements leads to non-linear phase behaviors, in agreement with results from the cubic simulations in Chapter 2. It was also shown how Gibb's ringing and low numbers of particles per voxel can also lead to non-linear phase as a function of echo time. The simulated random arrangements and most experiments did agree with the static dephasing theoretical shift at shorter echo times. Phase outside the cylinder containing discrete particles where no near-fields from particles exist behaved as if the cylinder was a continuous medium. It was also shown that the bulk susceptibility of the cylinder can be accurately quantified using the CISSCO method. In 4 this concept of using outside phase as an accurate reflection of bulk susceptibility was applied to clusters of iron-tagged stem cells. It was shown that the magnetic moment of each cluster can be used to

determine the number of cells in there. An improvement to the CISSCO method by using the magnitude squared of the complex signal rather than the real part was also developed.

The main focus in this thesis was to show that proper modeling of susceptibility microstructures may be necessary in some cases to predict MRI signal behaviors, even when such microstructures consist of simple spheres. However, the phase outside an object of interest with such microstructures still behaves as if the object consists of a uniform susceptibility. Thus phase outside the object is better to be used for the quantification of bulk susceptibility, as the detailed microstructures do not need to be taken into account.

Formulas from literature suggest that the iron oxide nanoparticle and water mixtures analyzed in Chapter 3 should be in the fast diffusion regime, meaning that no additional phase shifts should occur inside the mixture, contradicting experimental results. One possible explanation is that clustering had led to effectively larger particle sizes and pushed the signal closer to the static dephasing regime. Similar contradictions of signal relaxation noted in past work on Ferritin [81] were later explained by cellular clustering of Ferritin [41], as increasing particle radius (i.e. approaching the static dephasing regime) will lead to increasing R_2^* and R_2, up a certain point where R_2^* will plateau and R_2 will decrease [16, 17]. Thus it is possible that both these additional phase shifts and increasing signal relaxation may be occurring *in vivo* as well due to cellular clustering. This could lead to systematic errors when quantifying iron in the brain using either R_2^*, R_2, or phase. On the other hand, a more detailed understand-

ing of these shifts could lead to new methods for quantifying the magnitude of particle clustering.

While phase results due to the random particle arrangements in cylinders seem to agree with the static dephasing theoretical shift, it is unclear why this is not the case with the cubic object simulated in Chapter 2. With a cube, a random particle arrangement still leads to a non-linear phase behavior as a function of echo time. This suggests that one cannot simply add the theoretical static dephasing frequency shift to the Lorentz sphere corrected theoretical frequency. It is also curious in Chapter 3 why the nanoparticle experiment with a 0.29 ppm bulk susceptibility perpendicular to the main field did not match with the results from random particle arrangements. It was found that a quasi-random particle arrangement actually does a better job predicting the phase in that case. This may be due to a less random particle arrangement, yet one would think this would be the case at higher concentrations as well.

Future work in this direction could involve simulations of other types of quasi-random particle arrangements or more complicated microstructures. In order to investigate why adding a shift term to a cube does not produce the same result as simulating randomly placed particles, it would be interesting to simulate other geometries and to determine when this shift agrees with theory. Diffusion could also be added to our simulations through the use of Monte Carlo simulations, as done in other work.

REFERENCES

[1] Haacke, E.M., Cheng, N.Y., House, M.J., Liu, Q., Neelavalli, J., Ogg, R.J., et al. Imaging iron stores in the brain using magnetic resonance imaging. Magn Reson Imaging 2005;23(1):1–25.

[2] Yablonskiy, D.A., Haacke, E.M.. Theory of nmr signal behavior in magnetically inhomogeneous tissues: the static dephasing regime. Magn Reson Med 1994;32(6):749–63.

[3] Roch, A., Muller, R.N., Gillis, P.. Theory of proton relaxation induced by superparamagnetic particles. The Journal of chemical physics 1999;110(11):5403–5411.

[4] Marques, J., Bowtell, R.. Application of a fourier-based method for rapid calculation of field inhomogeneity due to spatial variation of magnetic susceptibility. Concepts in Magnetic Resonance Part B: Magnetic Resonance Engineering 2005;25(1):65–78.

[5] Cheng, Y.C., Hsieh, C.Y., Neelavalli, J., Haacke, E.M.. Quantifying effective magnetic moments of narrow cylindrical objects in mri. Phys Med Biol 2009;54(22):7025–44.

[6] Cheng, Y.C., Hsieh, C.Y., Tackett, R., Kokeny, P., Regmi, R.K., Lawes, G.. Magnetic moment quantifications of small spherical objects in mri. Magn Reson Imaging 2015;33(6):829–39.

[7] He, X., Yablonskiy, D.A.. Biophysical mechanisms of phase contrast in gradient echo mri. Proc Natl Acad Sci U S A 2009;106(32):13558–63.

[8] Chen, W.C., Foxley, S., Miller, K.L.. Detecting microstructural properties

of white matter based on compartmentalization of magnetic susceptibility. Neuroimage 2013;70:1–9.

[9] Luo, J., He, X., Yablonskiy, D.A.. Magnetic susceptibility induced white matter mr signal frequency shifts–experimental comparison between lorentzian sphere and generalized lorentzian approaches. Magn Reson Med 2014;71(3):1251–63.

[10] Duyn, J.. Mr susceptibility imaging. J Magn Reson 2013;229:198–207.

[11] Matsumoto, Y., Jasanoff, A.. T2 relaxation induced by clusters of superparamagnetic nanoparticles: Monte carlo simulations. Magn Reson Imaging 2008;26(7):994–8.

[12] Hak, S., Goa, P.E., Stenmark, S., Bjerkholt, F.F., Haraldseth, O.. Transverse relaxivity of iron oxide nanocrystals clustered in nanoemulsions: Experiment and theory. Magn Reson Med 2015;74(3):858–67.

[13] Ruh, A., Scherer, H., Kiselev, V.G.. The larmor frequency shift in magnetically heterogeneous media depends on their mesoscopic structure. Magn Reson Med 2018;79(2):1101–1110.

[14] Kokeny, P., Cheng, Y.N., Xie, H.. A study of mri gradient echo signals from discrete magnetic particles with considerations of several parameters in simulations. Magn Reson Imaging 2018;48:129–137.

[15] Kokeny, P., Cheng, Y.N., Liu, S., Xie, H., Jiang, Q.. Quantifications of in vivo labeled stem cells based on measurements of magnetic moments. Magn Reson Imaging 2017;35:141–147.

[16] Muller, R.N., Gillis, P., Moiny, F., Roch, A.. Transverse relaxivity of

particulate mri contrast media: from theories to experiments. Magn Reson Med 1991;22(2):178–82; discussion 195–6.

[17] Weisskoff, R.M., Zuo, C.S., Boxerman, J.L., Rosen, B.R.. Microscopic susceptibility variation and transverse relaxation: theory and experiment. Magn Reson Med 1994;31(6):601–10.

[18] Salomir, R., de Senneville, B.D., Moonen, C.T.. A fast calculation method for magnetic field inhomogeneity due to an arbitrary distribution of bulk susceptibility. Concepts in Magnetic Resonance Part B: Magnetic Resonance Engineering 2003;19(1):26–34.

[19] Durrant, C., Hertzberg, M., Kuchel, P.. Magnetic susceptibility: further insights into macroscopic and microscopic fields and the sphere of lorentz. Concepts in Magnetic Resonance Part A 2003;18(1):72–95.

[20] Chen, Z., Calhoun, V.. Nonlinear magnitude and linear phase behaviors of t2* imaging: theoretical approximation and monte carlo simulation. Magn Reson Imaging 2015;33(4):390–400.

[21] Pintaske, J., Muller-Bierl, B., Schick, F.. Effect of spatial distribution of magnetic dipoles on lamor frequency distribution and mr signal decay–a numerical approach under static dephasing conditions. MAGMA 2006;19(1):46–53.

[22] Xie, H., Cheng, Y.C.N., Kokeny, P., Liu, S., Hsieh, C.Y., Haacke, E.M., et al. A quantitative study of susceptibility and additional frequency shift of three common materials in mri. Magnetic resonance in medicine 2016;76(4):1263–1269.

[23] Kuipers, L., Niederreiter, H.. Uniform distribution of sequences. Mineola, N.Y.: Dover Publications; 2006. ISBN 0486450198 (pbk.).

[24] Bowen, C.V., Zhang, X., Saab, G., Gareau, P.J., Rutt, B.K.. Application of the static dephasing regime theory to superparamagnetic iron-oxide loaded cells. Magn Reson Med 2002;48(1):52–61.

[25] Butts, K., Sinclair, J., Daniel, B.L., Wansapura, J., Pauly, J.M.. Temperature quantitation and mapping of frozen tissue. J Magn Reson Imaging 2001;13(1):99–104.

[26] Wang, Y., Liu, T.. Quantitative susceptibility mapping (qsm): decoding mri data for a tissue magnetic biomarker. Magnetic resonance in medicine 2015;73(1):82–101.

[27] Haacke, E.M., Liu, S., Buch, S., Zheng, W., Wu, D., Ye, Y.. Quantitative susceptibility mapping: current status and future directions. Magnetic resonance imaging 2015;33(1):1–25.

[28] Wharton, S., Bowtell, R.. Fiber orientation-dependent white matter contrast in gradient echo mri. Proc Natl Acad Sci U S A 2012;109(45):18559–64.

[29] Duyn, J.H., Barbara, T.M.. Sphere of lorentz and demagnetization factors in white matter. Magn Reson Med 2014;72(1):1–3.

[30] Jackson, J.D.. Classical electrodynamics. John Wiley & Sons; 2012.

[31] Weisskoff, R.M., Kiihne, S.. Mri susceptometry: image-based measurement of absolute susceptibility of mr contrast agents and human blood. Magnetic resonance in medicine 1992;24(2):375–383.

[32] Krevelen, D.W.v.. Properties of polymers : their correlation with chemical structure, their numerical estimation and prediction from additive group contributions. 3rd, completely rev. ed.; Amsterdam ; New York: Elsevier; 1990. ISBN 0444881603.

[33] De Rochefort, L., Brown, R., Prince, M.R., Wang, Y.. Quantitative mr susceptibility mapping using piece-wise constant regularized inversion of the magnetic field. Magnetic Resonance in Medicine: An Official Journal of the International Society for Magnetic Resonance in Medicine 2008;60(4):1003–1009.

[34] Schweser, F., Zivadinov, R.. Quantitative susceptibility mapping (qsm) with an extended physical model for mri frequency contrast in the brain: a proof-of-concept of quantitative susceptibility and residual (quasar) mapping. NMR in Biomedicine 2018;:e3999.

[35] Liu, C.. Susceptibility tensor imaging. Magnetic Resonance in Medicine: An Official Journal of the International Society for Magnetic Resonance in Medicine 2010;63(6):1471–1477.

[36] Cronin, M.J., Bowtell, R.. Quantifying mri frequency shifts due to structures with anisotropic magnetic susceptibility using pyrolytic graphite sheet. Scientific reports 2018;8(1):6259.

[37] Duyn, J.H.. Studying brain microstructure with magnetic susceptibility contrast at high-field. Neuroimage 2018;168:152–161.

[38] Duyn, J.H., Schenck, J.. Contributions to magnetic susceptibility of brain tissue. NMR in Biomedicine 2017;30(4):e3546.

[39] Rudko, D.A., Klassen, L.M., de Chickera, S.N., Gati, J.S., Dekaban, G.A., Menon, R.S.. Origins of r2* orientation dependence in gray and white matter. Proc Natl Acad Sci U S A 2014;111(1):E159–67.

[40] Kiselev, V.G., Novikov, D.S.. Transverse nmr relaxation in biological tissues. Neuroimage 2018;.

[41] Gossuin, Y., Gillis, P., Muller, R.N., Hocq, A.. Relaxation by clustered ferritin: a model for ferritin-induced relaxation in vivo. NMR in Biomedicine: An International Journal Devoted to the Development and Application of Magnetic Resonance In vivo 2007;20(8):749–756.

[42] Brammerloh, M., Weigelt, I., Arendt, T., Gavriilidis, F., Scherf, N., Jankuhn, S., et al. Iron-induced relaxation mechanisms in the human substantia nigra: toward quantifying iron load in dopaminergic neurons. In: Proc 27th Annu Meeting ISMRM. 2018, p. 0188.

[43] Xie, H., Cheng, Y.C.N., Liu, S., Kokeny, P.. Removing unwanted background phase with a reference phantom for applications in susceptibility quantification. Magnetic resonance imaging 2018;54:32–45.

[44] Zhang, Z.G., Chopp, M.. Neurorestorative therapies for stroke: underlying mechanisms and translation to the clinic. Lancet Neurol 2009;8(5):491–500.

[45] Li, Y., Chopp, M.. Marrow stromal cell transplantation in stroke and traumatic brain injury. Neurosci Lett 2009;456(3):120–3.

[46] Aghayan, H.R., Arjmand, B., Yaghoubi, M., Moradi-Lakeh, M., Kashani, H., Shokraneh, F.. Clinical outcome of autologous mononuclear cells

transplantation for spinal cord injury: a systematic review and meta-analysis. Med J Islam Repub Iran 2014;28:112.

[47] Doeppner, T.R., Hermann, D.M.. Stem cell-based treatments against stroke: observations from human proof-of-concept studies and considerations regarding clinical applicability. Front Cell Neurosci 2014;8:357.

[48] Dunnett, S.B., Bjorklund, A., Lindvall, O.. Cell therapy in parkinson's disease - stop or go? Nat Rev Neurosci 2001;2(5):365–9.

[49] Jiang, Q., Zhang, Z.G., Ding, G.L., Silver, B., Zhang, L., Meng, H., et al. Mri detects white matter reorganization after neural progenitor cell treatment of stroke. Neuroimage 2006;32(3):1080–9.

[50] Jiang, Q., Zhang, Z.G., Ding, G.L., Zhang, L., Ewing, J.R., Wang, L., et al. Investigation of neural progenitor cell induced angiogenesis after embolic stroke in rat using mri. Neuroimage 2005;28(3):698–707.

[51] Hoehn, M., Kustermann, E., Blunk, J., Wiedermann, D., Trapp, T., Wecker, S., et al. Monitoring of implanted stem cell migration in vivo: a highly resolved in vivo magnetic resonance imaging investigation of experimental stroke in rat. Proc Natl Acad Sci U S A 2002;99(25):16267–72.

[52] Bulte, J.W., Duncan, I.D., Frank, J.A.. In vivo magnetic resonance tracking of magnetically labeled cells after transplantation. J Cereb Blood Flow Metab 2002;22(8):899–907.

[53] Frank, J.A., Miller, B.R., Arbab, A.S., Zywicke, H.A., Jordan, E.K., Lewis, B.K., et al. Clinically applicable labeling of mammalian and stem cells by combining superparamagnetic iron oxides and transfection agents.

Radiology 2003;228(2):480–7.

[54] Bulte, J.W., Kraitchman, D.L.. Iron oxide mr contrast agents for molecular and cellular imaging. NMR Biomed 2004;17(7):484–99.

[55] Bulte, J.W., Ben-Hur, T., Miller, B.R., Mizrachi-Kol, R., Einstein, O., Reinhartz, E., et al. Mr microscopy of magnetically labeled neurospheres transplanted into the lewis eae rat brain. Magn Reson Med 2003;50(1):201–5.

[56] Bulte, J.W., De Cuyper, M.. Magnetoliposomes as contrast agents. Methods Enzymol 2003;373:175–98.

[57] Bulte, J.W., Douglas, T., Witwer, B., Zhang, S.C., Strable, E., Lewis, B.K., et al. Magnetodendrimers allow endosomal magnetic labeling and in vivo tracking of stem cells. Nat Biotechnol 2001;19(12):1141–7.

[58] Frank, J.A., Anderson, S.A., Kalsih, H., Jordan, E.K., Lewis, B.K., Yocum, G.T., et al. Methods for magnetically labeling stem and other cells for detection by in vivo magnetic resonance imaging. Cytotherapy 2004;6(6):621–5.

[59] Arbab, A.S., Yocum, G.T., Kalish, H., Jordan, E.K., Anderson, S.A., Khakoo, A.Y., et al. Efficient magnetic cell labeling with protamine sulfate complexed to ferumoxides for cellular mri. Blood 2004;104(4):1217–23.

[60] Arbab, A.S., Yocum, G.T., Rad, A.M., Khakoo, A.Y., Fellowes, V., Read, E.J., et al. Labeling of cells with ferumoxides-protamine sulfate complexes does not inhibit function or differentiation capacity of hematopoietic or mesenchymal stem cells. NMR Biomed 2005;18(8):553–9.

[61] Janowski, M., Walczak, P., Kropiwnicki, T., Jurkiewicz, E., Domanska-Janik, K., Bulte, J.W., et al. Long-term mri cell tracking after intraventricular delivery in a patient with global cerebral ischemia and prospects for magnetic navigation of stem cells within the csf. PLoS One 2014;9(2):e97631.

[62] Bulte, J.W.. In vivo mri cell tracking: clinical studies. AJR Am J Roentgenol 2009;193(2):314–25.

[63] Bizzi, A., Brooks, R.A., Brunetti, A., Hill, J.M., Alger, J.R., Miletich, R.S., et al. Role of iron and ferritin in mr imaging of the brain: a study in primates at different field strengths. Radiology 1990;177(1):59–65.

[64] Vymazal, J., Brooks, R.A., Patronas, N., Hajek, M., Bulte, J.W., Di Chiro, G.. Magnetic resonance imaging of brain iron in health and disease. J Neurol Sci 1995;134 Suppl:19–26.

[65] Vymazal, J., Brooks, R.A., Baumgarner, C., Tran, V., Katz, D., Bulte, J.W., et al. The relation between brain iron and nmr relaxation times: an in vitro study. Magn Reson Med 1996;35(1):56–61.

[66] Vymazal, J., Hajek, M., Patronas, N., Giedd, J.N., Bulte, J.W., Baumgarner, C., et al. The quantitative relation between t1-weighted and t2-weighted mri of normal gray matter and iron concentration. J Magn Reson Imaging 1995;5(5):554–60.

[67] Schenker, C., Meier, D., Wichmann, W., Boesiger, P., Valavanis, A.. Age distribution and iron dependency of the t2 relaxation time in the globus pallidus and putamen. Neuroradiology 1993;35(2):119–24.

[68] Ordidge, R.J., Gorell, J.M., Deniau, J.C., Knight, R.A., Helpern, J.A.. Assessment of relative brain iron concentrations using t2-weighted and t2*-weighted mri at 3 tesla. Magn Reson Med 1994;32(3):335–41.

[69] Zelivyanskaya, M.L., Nelson, J.A., Poluektova, L., Uberti, M., Mellon, M., Gendelman, H.E., et al. Tracking superparamagnetic iron oxide labeled monocytes in brain by high-field magnetic resonance imaging. J Neurosci Res 2003;73(3):284–95.

[70] Mowat, P., Franconi, F., Chapon, C., Lemaire, L., Dorat, J., Hindre, F., et al. Evaluating spio-labelled cell mr efficiency by three-dimensional quantitative t2* mri. NMR Biomed 2007;20(1):21–7.

[71] Athiraman, H., Jiang, Q., Ding, G.L., Zhang, L., Zhang, Z.G., Wang, L., et al. Investigation of relationships between transverse relaxation rate, diffusion coefficient, and labeled cell concentration in ischemic rat brain using mri. Magn Reson Med 2009;61(3):587–94.

[72] Del Gratta, C., Della Penna, S., Battista, P., Di Donato, L., Vitullo, P., Romani, G.L., et al. Detection and counting of specific cell populations by means of magnetic markers linked to monoclonal antibodies. Phys Med Biol 1995;40(4):671–81.

[73] Ogg, R.J., Langston, J.W., Haacke, E.M., Steen, R.G., Taylor, J.S.. The correlation between phase shifts in gradient-echo mr images and regional brain iron concentration. Magn Reson Imaging 1999;17(8):1141–8.

[74] Shen, Y., Cheng, Y.C., Lawes, G., Neelavalli, J., Sudakar, C., Tackett, R., et al. Quantifying magnetic nanoparticles in non-steady flow by mri.

MAGMA 2008;21(5):345–56.

[75] Jung, C.W., Jacobs, P.. Physical and chemical properties of superparamagnetic iron oxide mr contrast agents: ferumoxides, ferumoxtran, ferumoxsil. Magn Reson Imaging 1995;13(5):661–74.

[76] Panizzo, R.A., Gadian, D.G., Sowden, J.C., Wells, J.A., Lythgoe, M.F., Ferretti, P.. Monitoring ferumoxide-labelled neural progenitor cells and lesion evolution by magnetic resonance imaging in a model of cell transplantation in cerebral ischaemia. F1000Res 2013;2:252.

[77] Heyn, C., Bowen, C.V., Rutt, B.K., Foster, P.J.. Detection threshold of single spio-labeled cells with fiesta. Magn Reson Med 2005;53(2):312–20.

[78] Verdijk, P., Scheenen, T.W., Lesterhuis, W.J., Gambarota, G., Veltien, A.A., Walczak, P., et al. Sensitivity of magnetic resonance imaging of dendritic cells for in vivo tracking of cellular cancer vaccines. Int J Cancer 2007;120(5):978–84.

[79] Shapiro, E.M., Skrtic, S., Sharer, K., Hill, J.M., Dunbar, C.E., Koretsky, A.P.. Mri detection of single particles for cellular imaging. Proc Natl Acad Sci U S A 2004;101(30):10901–6.

[80] Heyn, C., Ronald, J.A., Mackenzie, L.T., MacDonald, I.C., Chambers, A.F., Rutt, B.K., et al. In vivo magnetic resonance imaging of single cells in mouse brain with optical validation. Magn Reson Med 2006;55(1):23–9.

[81] Wood, J.C., Fassler, J.D., Meade, T.. Mimicking liver iron overload using liposomal ferritin preparations. Magnetic Resonance in Medicine: An Official Journal of the International Society for Magnetic Resonance in

Medicine 2004;51(3):607–611.

ABSTRACT

STUDY OF MRI SIGNAL ARISING FROM DISCRETE SPHERICAL PARTICLES

by

PAUL KOKENY

December 2018

Co-Advisor: Dr. Yu-Chung Norman Cheng

Co-Advisor: Dr. E Mark Haacke

Major: Biomedical Engineering (imaging dual title)

Degree: Doctor of Philosophy

Simulating signal behavior in Magnetic Resonance imaging (MRI) is often a necessary step in being able to understand how signal relates to certain physiological parameters. One such parameter of interest in the body is magnetic susceptibility since it is related to iron content. The bulk magnetic susceptibility of an object is a property that describes how magnetized it becomes when placed in an external magnetic field. When the bulk susceptibility of an object arises from the presence of discrete magnetic inclusions, the MRI phase signal inside the object can no longer be determined analytically by assuming it has a continuous susceptibility. This phase will depend on the microstructure of the inclusions and requires either simulations or some other analytical modeling which makes assumptions about the microstructure. Under static dephasing conditions, if the discrete inclusions are spherical particles and randomly dispersed, then a known frequency shift will affect the phase signal. It has also recently been shown that this shift can vary depending on the volume fraction and clustering of the particles. The main focus dissertation is to demonstrate

that spherical particles inside an object can lead to non-linear phase behavior which is not describable by a signal frequency shift, while the phase outside the object behaves as if it were continuous. This makes the phase outside the object a more reliable source for susceptibility quantification, as it does not depend on the microstructure of the object.

This dissertation consists of three major research projects. The first explores different static dephasing simulation model parameters to predict MRI phase from different quasi-random arrangements of spherical particles. Guidelines are established on the required size of the modeled particles and how many are needed per simulated MRI voxel to obtain precise and accurate results. It is also shown how restricting the randomness of particles affects the simulated voxel phase and $R_2^{'}$ values. The second research project uses these guidelines to simulate long cylinders made up of discrete spherical particles. Both random and quasi-random particle arrangements were used. Input parameters for these simulations were taken from experimental phantom data which also consisted of cylinders that contain mixtures of nanoparticles and polystyrene beads, separately. Phase inside the cylinders, bulk susceptibility quantified from phase outside them, and $R_2^{'}$ were compared between simulation and experiment. In most cases, the averaged phase inside the simulated and experimental cylinders agree with the theoretical shift for static dephasing regime, while one experimental case agrees better with the quasi-random arrangement. The predicted large variation of phase values from having low numbers or particles per voxel was seen in experiment. The $R_2^{'}$ from simulations was generally higher than

the quantified R_2^* from experiment. Bulk susceptibilities of simulated and experimental cylinders were in good agreement and shown to be insensitive to particle arrangement. This supports the reliability of using outside phase for quantification. In the third research project, this concept of using outside phase as an accurate reflection of bulk susceptibility was applied to clusters of iron-tagged stem cells. It was shown how the magnetic moment of the cluster should can be used to determine the number of cells there.

AUTOBIOGRAPHICAL STATEMENT

Name: Paul Kokeny

Education:

Ph.D. Biomedical Engineering, Wayne State University, Detroit, MI, USA, 2013 - Present
M.S. Biomedical Engineering, Wayne State University, Detroit, MI, USA, 2013
B.S. Electrical Engineering, Western Michigan University, Kalamazoo, MI, 2008

Work Experience:

Research and Student Assistant, Wayne State University, Detroit, MI, USA, 2012-present
Data Processor, MR Innovations Inc, Detroit, MI, USA, 2011-2012
Process Engineer, Belmont Equipment, Madison Heights, MI, USA, 2008-2011

Publications:

P Kokeny, YCN Cheng, H Xie. Mixtures of discrete spherical particles with a constant susceptibility can lead to echo time dependent phase shifts. *Magnetic resonance in medicine* 2018 (in progress)

H Xie, YCN Cheng, S Liu, **P Kokeny**. Removing unwanted background phase with a reference phantom for applications in susceptibility quantification. *Magnetic resonance imaging*, 54: 32-45, 2018

P Kokeny, YCN Cheng, H Xie. A study of MRI gradient echo signals from discrete magnetic particles with considerations of several parameters in simulations. *Magnetic resonance imaging* 48: 129-137, 2018

P Kokeny, YCN Cheng, S Liu, H Xie, Q Jiang. Quantifications of in vivo labeled stem cells based on measurements of magnetic moments. *Magnetic resonance imaging* 35: 141-147, 2017

H Xie, YCN Cheng, **P Kokeny**, S Liu, CY Hsieh, EM Haacke, M Arachchige, G Lawes. A quantitative study of susceptibility and additional frequency shift of three common materials in MRI. *Magnetic resonance in medicine* 76: 1263-1269, 2016

YCN Cheng, CY Hsieh, R Tackett, **P Kokeny**, RK Regmi, G Lawes. Magnetic Moment quantifications of small spherical objects in MRI. *Magnetic resonance imaging* 33(6): 829-839, 2015

J Jiang, **P Kokeny**, W Ying, C Magnano, R Zivadinov, EM Haacke. Quantifying errors in flow measurements using phase contrast magnetic resonance imaging: comparison of several boundary detection methods. *Magnetic resonance in medicine* 33(2): 185-193, 2014

MM Lagana, A Chaudhary, D Balagurunathan, D Utriainen, **P Kokeny**, W Feng, P Cecconi, D Hubbard, EM Haacke. Cerebrospinal fluid flow dynamics in multiple sclerosis patients through phase contrast magnetic resonance imaging. *Curr Neurovasc Res.* 11(4): 349-358, 2014